The Astrophysical Journal, 949:101 (30pp), 2023 June 1 https://doi.org/10.3847/1538-4357/acc94a

RAIKOU (来光): A General Relativistic, Multiwavelength Radiative Transfer Code

Tomohisa Kawashima[1], Ken Ohsuga[2], and Hiroyuki R. Takahashi[3]
[1] Institute for Cosmic Ray Research, The University of Tokyo, 5-1-5 Kashiwanoha, Kashiwa, Chiba 277-8582, Japan; kawshm@icrr.u-tokyo.ac.jp
[2] Center for Computational Sciences, University of Tsukuba, Ten-nodai, 1-1-1 Tsukuba, Ibaraki 305-8577, Japan
[3] Department of Natural Sciences, Faculty of Arts and Sciences, Komazawa University, 1-23-1 Komazawa, Setagaya, Tokyo 154-8525, Japan
Received 2023 February 10; revised 2023 March 18; accepted 2023 March 29; published 2023 June 2

Abstract

We present a general relativistic radiative transfer code RAIKOU (来光) for multiwavlength studies of spectra and images including the black hole shadows around Kerr black holes. Important radiative processes in hot plasmas around black holes, i.e., (cyclo-)synchrotron, bremsstrahlung emission/absorption, and Compton/inverse-Compton scattering, are incorporated. The Maxwell–Jüttner and single/broken power-law electron distribution functions are implemented to calculate the radiative transfer via both thermal and nonthermal electrons. Two calculation algorithms are implemented for studies of the images and broadband spectra. An observer-to-emitter ray-tracing algorithm, which inversely solves the radiative transfer equation from the observer screen to emitting plasmas, is suitable for an efficient calculations of the images, e.g., the black hole shadows observed by the Event Horizon Telescope, and spectra without Compton effects. On the other hand, an emitter-to-observer Monte Carlo algorithm, by which photons are transported with a Monte Carlo method including the effects of Compton/inverse-Compton scatterings, enables us to compute multiwavelength spectra, with their energy bands broadly ranging from radio to very high energy gamma-ray. The X-ray black hole shadows, which are formed via synchrotron emission and inverse-Compton scattering processes and will be observed in the future X-ray interferometry missions, can be also computed with this algorithm. The code is generally applicable to accretion flows around Kerr black holes with relativistic jets and winds/coronae with various mass accretion rates (i.e., radiatively inefficient accretion flows, super-Eddington accretion flows, and others). We demonstrate an application of the code to a radiatively inefficient accretion flow onto a supermassive black hole.

Unified Astronomy Thesaurus concepts: Black hole physics (159); General relativity (641); Radiative transfer (1335); Accretion (14); Relativistic jets (1390); High energy astrophysics (739); Computational methods (1965)

1. Introduction

Astrophysical black holes (BHs) are thought to be powered by the gravitational energy release via the accretion flows. The energy release in the accretion flows will result in the emission of an enormous amount of electromagnetic radiation (e.g., Shakura & Sunyaev 1973; Abramowicz et al. 1988; Narayan & Yi 1994) and the ejection of powerful outflows (i.e., relativistic jets and mildly relativistic winds), which are theoretically suggested to be accelerated by magnetic processes (Blandford & Znajek 1977; Blandford & Payne 1982; Lynden-Bell 1996), and radiative force (Sikora 1981). In order to study BH spacetimes and physics of these plasma dynamics, computations of general relativistic radiative transfer (GRRT) will be a powerful tool, because GRRT calculations of images and spectra will enable us to directly compare the theoretical models with the observed data.

One of the most important observable features of BHs is their shadows or silhouettes (Bardeen 1973; Luminet 1979; Falcke et al. 2000; Takahashi 2004; Broderick & Loeb 2006; Noble et al. 2007; Dexter et al. 2012; Chan et al. 2015; Mościbrodzka et al. 2016; Chael et al. 2018), because their images are formed as a consequence of the significant light-bending effect due to the extremely strong gravity of the BHs. Recently, the Event Horizon Telescope (EHT) detected the image of a BH shadow in the elliptical galaxy M87* (Event Horizon Telescope Collaboration et al. 2019a, 2019b, 2019c, 2019d, 2019e, 2019f), and this provided strong and important evidence of supermassive BHs (SMBHs), whose formation scenario is still controversial (Rees 1984; Volonteri 2012).

The diameter of the observed photon ring, which is a bright ring image formed by the photons passing through near the unstable photon orbit around the BHs, is $\sim$40 μas (Event Horizon Telescope Collaboration 2019d). The BH mass can be estimated to be $6.5 \times 10^9 M_\odot$ (Event Horizon Telescope Collaboration 2019f) because the diameter of the photon ring is roughly proportional to the BH mass, i.e., $\sim 10 r_g$, where r_g is the gravitational radius defined as $r_g \equiv GM/c^2$, G is the gravitaional constant, M is the BH mass, and c is the speed of light. However, constraining the BH spin is still a great challenge because the diameter of the photon ring depends weakly on the BH spin. In practice, the diameter changes within $\pm 5\%$ (e.g., Psaltis et al. 2015), and it would be difficult to identify using the current EHT. In addition, the dynamics of accretion flows and launching mechanism of jets are still enigmatic. It would therefore be important to explore these problems using an additional feature, e.g., polarization (Broderick & Loeb 2006; Shcherbakov et al. 2012; Dexter 2016; Gold et al. 2017; Mościbrodzka et al. 2017; Tsunetoe et al. 2020; Event Horizon Telescope Collaboration et al. 2021; Tsunetoe et al. 2021), and/or multiwavelength spectra (Ohsuga et al. 2005; Mościbrodzka et al. 2009; Chael et al. 2016; Mościbrodzka et al. 2016; Chael et al. 2018). The latter approach is the motivation for the code we develop in this paper.

The multi-wevelength radiative transfer calculations, whose energy band ranges from radio to very high energy (VHE) gamma-rays, potentially constrain the various parameters with respect to BH spacetimes and theoretical models of the accretion flows and jets via the simultaneous comparison between theoretical and observed radiative flux in the various energy bands. In order to calculate the spectral energy distributions (SEDs) of accretion flows and jets around BHs above the X-ray band, it is necessary to incorporate the effects of Compton and inverse-Compton scattering (e.g., Rybicki & Lightman 1979). For the calculations of the Comptonized SEDs, Monte Carlo (MC) radiative transfer (e.g., Pozdnyakov et al. 1977, 1983; Gorecki & Wilczewski 1984; Canfield et al. 1987; Dolence et al. 2009) is suitable for accurate computations of the Compton/inverse-Compton scattering without introducing approximations (e.g., the Kompaneets approximation, which is applicable when the radiative field is isotropic in the fluid rest frame; Kompaneets 1957), although the MC calculations are computationally costly.

Although most previous works on GRRT calculations focused on thermal electrons, the observations of BHs strongly demonstrate the evidence of the acceleration of electrons. For example, the VHE gamma-ray observation of M87 by the MAGIC Telescope indicates the generation of nonthermal electrons at a distance of $\sim 100 r_{\rm g}$ from the BH in M87 (MAGIC Collaboration et al. 2020). The recent simultaneous multi-wavelength observation campaign for EHT 2017 found that the gamma-ray emission is not generated at the same place as the ring emission in the vicinity of the BH when an isotropic distribution of the nonthermal electrons is assumed (EHT MWL Science Working Group et al. 2021). On the other hand, IC 310 shows subday-scale rapidly varying VHE gamma-ray emission, which is interpreted as emission that orginated from the nonthermal electrons that were accelerated from the gap electric field in the vinicity of the BH (Aleksić et al. 2014). In the lower frequency bands, the synchrotron emission via nonthermal electrons can reproduce the radio emission at $\nu < 100$ GHz (Yuan et al. 2003; Davelaar et al. 2018), and it will be important to consider the images and spectra at 230 GHz, infrared, and X-ray bands in Sgr A* (e.g., Ball et al. 2016; Chael et al. 2017; Mao et al. 2017; Chatterjee et al. 2021; Scepi et al. 2022).

Calculations of the Comptonized SEDs are important for general studies of BHs, whose mass ranges from stellar mass BHs to SMBHs, with the mass accretion rate ranging from sub-Eddington to super-Eddington. For example, in the super-Eddington accretion flows, the Compton/inverse-Compton scattering in jets and winds drastically modifies the SEDs (Kawashima et al. 2012; Kitaki et al. 2017; Narayan et al. 2017; Curd & Narayan 2019; Kawanaka & Mineshige 2021), which will be important to explain the SEDs of ultraluminous X-ray sources (ULXs) and tidal disruption events (TDEs). The origin of the hard X-ray photons from the BH accretion flows with a marginally Eddington accretion rate, which is an open question and is proposed to be Comptonized in hot coronae that form above the standard disks or inside the truncated accretion disks, can be also approached (Kawanaka et al. 2008; Davis et al. 2009; Schnittman et al. 2013).

In this paper, we describe our newly developed general relativistic multiwavelength radiative transfer code RAIKOU (来光), by which the multiwavelength SEDs from radio to VHE gamma-ray bands and images of the BH shadow, accretion flows, and outflows can be calculated. The electron distribution functions of the thermal electrons with the Maxwell–Jüttner distribution and the nonthermal electrons with single/broken power-law distributions are incorporated. The VHE gamma-ray emission above TeV energy bands can be computed because of the implement of the inverse-Compton scattering processes via nonthermal electrons. The code can calculate the images and spectra of accreting BHs by postprocessing general relativisitic (radiation-)magnetohydrodynamic simulations, hereafter GR(R)MHD, as well as using semianalytic models. In Sections 2–5, the formalism and numerical method are described. In Section 6, numerical tests are shown. In Section 7, we demonstrate an application of the code to calculations of multiwavelength images and spectra of a radiatively inefficient accretion flow (hereafter RIAF; e.g., Yuan & Narayan 2014) onto Sgr A* based on GRMHD simulations. We devote Section 8 to the summary and discussion.

2. Overview of the Method

We describe the formalism of equations and algorithms implemented in RAIKOU. For the various purposes of the radiative transfer calculations, two types of calculation algorithm are employed. One is the observer-to-emitter ray-tracing (RT) algorithm, by which the radiative transfer equations are integrated from the observer screen to the emitting plasma. This method enables us to efficiently compute the accurate images and spectra in the limit of plasmas being optically thin against the inverse-Compton scattering. The other is the emitter-to-observer Monte Carlo (MC) algorithm, by which the superphotons are transported from the emitting plasma to the observer with an MC method. With the emitter-to-observer MC algorithm, one can compute broadband spectra from radio to VHE gamma-rays, which are significantly affected by Compton/inverse-Compoton scattering.

The same formalism and algorithm as for the ray-tracing part, i.e., the integration module of the geodesic equations of photons, are used for the observer-to-emitter RT and the emitter-to-observer MC algorithm. The details of the radiative transfer part including various radiative processes, i.e., the emission, abosorption, and scattering, are presented in the subsequent subsections.

3. Geodesics

We integrate the Hamilton canonical equations of motion, which describe the time evolution of the position and momentum of photons r, θ, φ, p_r, and p_θ in Boyer–Lindquist (BL) coordinates, to solve the geodesic equations for the photons (Schnittman & Krolik 2013). We do not solve the time evolution of the conserved variable of photons, i.e., time and azimuthal components of photons p_t and p_φ during the calculation of the geodesics, while these are updated when the photons are scattered via the Compton process.

The metric of the BL coordinate is written as follows:

$$g_{\mu\nu} = \begin{pmatrix} -\alpha^2 + \omega^2\varpi^2 & 0 & 0 & -\omega\varpi^2 \\ 0 & \rho^2/\Delta & 0 & 0 \\ 0 & 0 & \rho^2 & 0 \\ -\omega\varpi^2 & 0 & 0 & \varpi^2 \end{pmatrix}, \quad (1)$$

where in the geometrical unit $G = c = 1$,

$$\rho^2 = r^2 + a^2\cos^2\theta, \tag{2}$$

$$\Delta = r^2 - 2Mr + a^2, \tag{3}$$

$$\alpha^2 = \frac{\rho^2\Delta}{\rho^2\Delta + 2Mr(a^2 + r^2)}, \tag{4}$$

$$\omega = \frac{2Mar}{\rho^2\Delta + 2Mr(a^2 + r^2)}, \tag{5}$$

$$\varpi^2 = \frac{\rho^2\Delta + 2Mr(a^2 + r^2)}{\rho^2}\sin^2\theta. \tag{6}$$

The Hamiltonian in the BL coordinate is described as

$$H(r, \theta, \varphi, p_r, p_\theta, p_\varphi) = -p_t = \omega p_\varphi + \alpha\left(\frac{\Delta}{\rho^2}p_r^2 + \frac{1}{\rho^2}p_\theta^2 + \frac{1}{\varpi^2}p_\varphi^2 + m^2\right)^{1/2}. \tag{7}$$

The Hamilton equations $dx^i/dt = \partial H/\partial_{pi}$ and $dp_i/dt = -\partial H/\partial x^i$ are then written as follows:

$$\frac{dr}{dt} = -\frac{p_r}{p_t + \omega p_\varphi}\frac{\alpha^2\Delta}{\rho^2}, \tag{8}$$

$$\frac{d\theta}{dt} = -\frac{p_\theta}{p_t + \omega p_\varphi}\frac{\alpha^2}{\rho^2}, \tag{9}$$

$$\frac{d\varphi}{dt} = \omega - \frac{p_\varphi}{p_t + \omega p_\varphi}\frac{\alpha^2}{\varpi^2}, \tag{10}$$

$$\frac{dp_r}{dt} = -\frac{\partial\omega}{\partial r}p_\varphi + \frac{p_t + \omega p_\varphi}{\alpha}\frac{\partial\alpha}{\partial r} + \frac{1}{2}\frac{\alpha^2}{p_t + \omega p_\varphi}\frac{\partial}{\partial r}\left(\frac{\Delta}{\rho^2}p_r^2 + \frac{1}{\rho^2}p_\theta^2 + \frac{1}{\varpi^2}p_\varphi^2\right), \tag{11}$$

$$\frac{dp_\theta}{dt} = -\frac{\partial\omega}{\partial\theta}p_\varphi + \frac{p_t + \omega p_\varphi}{\alpha}\frac{\partial\alpha}{\partial\theta} + \frac{1}{2}\frac{\alpha^2}{p_t + \omega p_\varphi}\frac{\partial}{\partial\theta}\left(\frac{\Delta}{\rho^2}p_r^2 + \frac{1}{\rho^2}p_\theta^2 + \frac{1}{\varpi^2}p_\varphi^2\right). \tag{12}$$

As is mentioned above, dp_φ/dt is not solved during the calculation of geodesics as p_φ is conserved to be variable in the axisymmetric spacetime. The coefficients in the above Hamilton equations are described as follows:

$$\frac{\partial\omega}{\partial r} = -\frac{\omega^2}{2Ma}\left[3r^2 + a^2(1 + \cos^2\theta) - \frac{a^4}{r^2}\cos^2\theta\right], \tag{13}$$

$$\frac{\partial\omega}{\partial\theta} = -\frac{\omega^2\sin\theta\cos\theta}{2Ma}\left(2Ma^2 - a^2r - \frac{a^4}{r}\right), \tag{14}$$

$$\frac{\partial\alpha}{\partial r} = \frac{1}{2\alpha}\frac{\partial\alpha^2}{\partial r}, \tag{15}$$

$$\frac{\partial\alpha}{\partial\theta} = \frac{1}{2\alpha}\frac{\partial\alpha^2}{\partial\theta}, \tag{16}$$

$$\frac{\partial\alpha^2}{\partial r} = -\alpha^4\left(\frac{2M}{\Delta\rho^2}\right)\left(\frac{a^4 - r^4}{\Delta} - \frac{2r^2a^2\sin^2\theta}{\rho^2}\right), \tag{17}$$

$$\frac{\partial\alpha^2}{\partial\theta} = -\alpha^4\left[\frac{4Ma^2r\sin\theta\cos\theta(r^2 + a^2)}{\Delta\rho^4}\right], \tag{18}$$

$$\frac{\partial}{\partial r}\left(\frac{1}{\varpi^2}\right) = -\frac{2\sin^2\theta}{\varpi^4} \times \left[r + \frac{Ma^2\sin^2\theta(a^2\cos^2\theta - r^2)}{\rho^4}\right], \tag{19}$$

$$\frac{\partial}{\partial\theta}\left(\frac{1}{\varpi^2}\right) = -\frac{2\sin\theta\cos\theta}{\varpi^4} \times \left[2Ma^2r\sin^2\theta\left(\frac{r^2 + a^2}{\rho^4} + \frac{1}{\rho^2}\right) + (r^2 + a^2)\right], \tag{20}$$

$$\frac{\partial}{\partial r}\left(\frac{\Delta}{\rho^2}\right) = \frac{2}{\rho^2}\left(r - M - \frac{r\Delta}{\rho^2}\right), \tag{21}$$

$$\frac{\partial}{\partial\theta}\left(\frac{\Delta}{\rho^2}\right) = \frac{2}{\rho^4}a^2\Delta\sin\theta\cos\theta, \tag{22}$$

$$\frac{\partial}{\partial r}\left(\frac{1}{\rho^2}\right) = -\frac{2r}{\rho^4}, \tag{23}$$

$$\frac{\partial}{\partial\theta}\left(\frac{1}{\rho^2}\right) = \frac{2}{\rho^4}a^2\sin\theta\cos\theta. \tag{24}$$

The above equations are integrated using an eigth-order embedded Runge–Kutta method with an adaptive stepsize control (e.g., Press et al. 2002).

4. Radiative Transfer (I): Observer-to-emitter RT Algorithmm

The covariant radiative transfer equations, which are expressed by a suitable formula for the time-reversed calculations, are solved when we use the observer-to-emitter RT algorithm.

The covariant radiative transfer equations without scattering are described as follows:

$$\frac{d\mathcal{I}}{d\tau_\nu} = -\mathcal{I} + \mathcal{S}, \tag{25}$$

where τ_ν is the optical depth for photons, with their frequency ν measured in the observer frame.

The invariant specific intensity $\mathcal{I}$ and source function $\mathcal{S}$ is written as

$$\mathcal{I} = \frac{I_\nu}{\nu^3}, \tag{26}$$

$$\mathcal{S} = \frac{\mathcal{J}}{\mathcal{A}}, \tag{27}$$

$$\mathcal{J} = \frac{j_{\nu(\mathrm{tot})}}{\nu^2}, \tag{28}$$

$$\mathcal{A} = \nu\alpha_{\nu(\mathrm{tot})}, \tag{29}$$

where $\mathcal{J}$ and $\mathcal{A}$ are the invariant emissivity and absorption coefficient, respectively.

The covariant radiative transfer Equation (25) leads to the equation that is convenient to be integrated from the observer to the emitter (Younsi et al. 2012; Pu et al. 2016b),

$$\frac{d\mathcal{I}}{d\tau_{\nu(\mathrm{a})}} = \mathcal{S}e^{-\tau_{\nu(\mathrm{a})}}, \tag{30}$$

where $\tau_{\nu(\mathrm{a})}$ is the optical depth for the absorption calculated from the observer to the emitter. In practice, the infinitesimal changes in the invariant quantity $\tau_{\nu(\mathrm{a})}$ calculated in our code, such as

$$d\tau_{\nu(\mathrm{a})} = \alpha^{(\mathrm{z})}_{\nu_\mathrm{z}} dl = \left(\frac{\nu_\mathrm{f}}{\nu_\mathrm{z}}\right)\alpha^{(\mathrm{f})}_{\nu_\mathrm{f}} dl, \tag{31}$$

where dl is the distance of photon propagation measured in the zero angular momentum observer (ZAMO; Bardeen et al. 1972) frame. In the ZAMO frame, the infinitesimal $dx^{\hat{\mu}}$ can be transformed from that in the BL coordinate dx^{μ} as

$$dx^{\hat{\mu}} = e^{\hat{\mu}}_{\mu} dx^{\mu}, \tag{32}$$

where

$$e^{\hat{\mu}}_{\mu} = \begin{pmatrix} \alpha & 0 & 0 & 0 \\ 0 & \rho/\sqrt{\Delta} & 0 & 0 \\ 0 & 0 & \rho & 0 \\ -\omega\Delta\sin\theta/\alpha & 0 & 0 & \varpi \end{pmatrix}. \tag{33}$$

Then, dl is obtained by $dl = \sqrt{(dx^{\hat{r}})^2 + (dx^{\hat{\theta}})^2 + (dx^{\hat{\varphi}})^2}$. Since the radiative transfer equation is not scale free, we should calculate dl in the physical unit, i.e., cgs units in the code, while the geodesic equations can be calculated with being normalized by the gravitational radius. We note that ν_f and ν_z are the photon frequency observed in the fluid rest and ZAMO frame, respectively. The covariant four-momentum of a photon in the ZAMO frame is calculated as

$$p_{\hat{\mu}} = e^{\mu}_{\hat{\mu}} p_{\mu}, \tag{34}$$

where p_μ is the covariant four-momentum in the BL coordinates, and

$$e^{\mu}_{\hat{\mu}} = \begin{pmatrix} 1/\alpha & 0 & 0 & \omega\alpha \\ 0 & \sqrt{\Delta}/\rho & 0 & 0 \\ 0 & 0 & 1/\rho & 0 \\ 0 & 0 & 0 & 1/\varpi \end{pmatrix}. \tag{35}$$

The covariant source function Equation (27) is calculated with the total emissivity and absorption coefficient described in the following subsection.

4.1. Emission and Absorption

Various emission mechanisms can be simultaneously incorporated by summing up each emissivity in the fluid rest frame:

$$j^{(\mathrm{f})}_{\nu_\mathrm{f}(\mathrm{tot})} = \sum j^{(\mathrm{f})}_{\nu_\mathrm{f}}, \tag{36}$$

where the detailed formulations of the emissivity of each radiative processes via thermal and nonthermal electrons are described in Appendix B.1

The absorption coefficient can be obtained by summing up those for each radiative process:

$$\alpha^{(\mathrm{f})}_{\nu_\mathrm{f}(\mathrm{tot})} = \sum \alpha^{(\mathrm{f})}_{\nu_\mathrm{f}}, \tag{37}$$

where the detailed descriptions of the absorption coefficients for the radiative processes via thermal and nonthermal electrons are shown in Appendix C.

We integrate the covariant radiative transfer equation from the observer to the emitter described as Equation (30) by substituting the total emissivity and absorption coefficient to the covariant form of radiative quantities desribed in Equations (27), (28), and (29).

4.2. Observer Screen

The observer screen is located at a distance far from the BH, e.g., $10^4 r_\mathrm{g}$ by default. Each ray incoming to the screen is assumed to be perpendicular to the surface of the screen. We inversely trace the photon that arises from the center of the pixel of the screen. We solve the radiative transfer with various photon frequencies at observer screen simultaneously during the ray-tracing calculations.

5. Radiative Transfer (II): Emitter-to-observer MC Algorithm

The emitter-to-observer MC algorithm is used to transport the photons, taking into account the effects of Compton/inverse-Compton scattering. For the MC calculations, pseudo-random numbers are generated with the Mersenne-Twister method.

Four reference frames are used in this method: (i) the observer frame (BL frame) is used for the ray-tracing, (ii) the ZAMO frame is basically used for the analysis, (iii) the fluid rest frame is used to calculate the emission and absorption coefficient, and (iv) the electron rest frame is used to computate the Compton scattering. For the transformation among (ii), (iii), and (iv), the Lorentz transformation is used because these are the tetrad frames.

5.1. Emission

To transport the photons with the MC method, computational particles representing the photons, so-called superphotons, are generated in the computation box. The weight of superphotons w, which is a dimensionless quantity, represents the ratio of the number density of real photons to superphotons in the phase-space generated in the unit time (e.g., Dolence et al. 2009),

$$\frac{1}{\sqrt{-g}}\frac{dN_\mathrm{real}}{dtd^3xd\nu d\Omega} = w\frac{1}{\sqrt{-g}}\frac{dN_\mathrm{super}}{dtd^3xd\nu d\Omega} = \left(\frac{\nu}{\nu_\mathrm{f}}\right)\frac{j^{(\mathrm{f})}_{\nu_\mathrm{f}}}{h\nu_\mathrm{f}}, \tag{38}$$

where N_real and N_super are the number of real photons and superphotons, respectively. Therefore, w can be described as

$$w = \frac{\sqrt{-g}\,\Delta t\Delta^3 x\Delta\ln\nu}{\bar{N}_\mathrm{super} h}\int j^{(\mathrm{f})}_{\nu_\mathrm{f}} d\Omega^{(\mathrm{f})}, \tag{39}$$

where $\bar{N}_\mathrm{super}$ is the number of superphotons per photon-frequency bin per computational cell. It should be noted that $\sqrt{-g}$, Δt, and $\Delta^3 x\, d\nu$ are defined in the observer frame, while $d\Omega^{(\mathrm{f})}$ is defined in the fluid rest frame.[4]

[4] This equation is the same as that in Dolence et al. (2009) because $j_\nu d\Omega = j^{(\mathrm{f})}_{\nu_\mathrm{f}} d\Omega^{(\mathrm{f})}$, where j_ν is the emissivity in the observer frame.

5.2. Absorption

The absorption processes reduce the weight of the superphoton as

$$w_{\rm new} = w \exp\left[-\Delta\tau_{\nu({\rm a})}\right], \tag{40}$$

where $w_{\rm new}$ is the updated value of the superphoton weight w after one time step, and $\Delta\tau_{\nu({\rm a})}$ is the optical depth for absorption per time step of the ray-tracing. The total absorption coefficient described by Equation (37) and the formulation of the optical depth in Equation (31) are used to evaluate $\Delta\tau_{\nu({\rm a})}$.

5.3. Scattering

The overview of the procedure for calculating the Compton scattering is as follows: (i) we calculate the optical depth for the Compton scattering $d\tau_{\nu({\rm s})}$ between the current and previous position of the superphoton, (ii) we evaluate the probability of Compton scattering from $d\tau_{\nu({\rm s})}$, and examine whether the scattering takes place at the current position with an MC method, (iii) the Compton scattering with the MC method is calculated if the scattering occurs, and (iv) we return to (i) after integrating the geodesic equation for one time step. Our procedure to solve the Compton scattering with an MC method is similar to that of Dolence et al. (2009), except that we incorporate the effect of the nonthermal electrons in addition to the thermal electrons.

5.3.1. Optical Depth for the Compton Scattering

The optical depth for the Compton scattering is computed taking into account the fluid motion and kinetic motion of thermal and nonthemal electrons,

$$d\tau_{\nu({\rm s})} = \frac{\nu_{\rm f}}{\nu_{\rm z}}\left(n_{\rm e,th}\sigma_{\rm KN,th} + n_{\rm e,nth}\sigma_{\rm KN,nth}\right)dl, \tag{41}$$

where $\sigma_{\rm KN,th}$ and $\sigma_{\rm KN,nth}$ are the Klein–Nishina cross section modified by taking into account the effect of the kinetic motion of thermal and nonthermal electrons in the fluid rest frame, respectively. We note that the former is the same as the hot cross section in Dolence et al. (2009). This modified cross section is formulated as

$$\begin{aligned}\sigma_{\rm KN,th} &= \frac{1}{n_{\rm e,th}}\int d^3p_{\rm e}\frac{dn_{\rm e,th}}{d^3p_{\rm e}}(1-\mu_{\rm e}\beta_{\rm e})\sigma_{\rm KN},\\ &= \frac{1}{2n_{\rm e,th}}\int d\gamma_{\rm e}\int d\mu_{\rm e}\frac{dn_{\rm e,th}}{d\gamma_{\rm e}}\\ &\quad (1-\mu_{\rm e}\sqrt{1-\gamma_{\rm e}^{-2}})\sigma_{\rm KN},\end{aligned} \tag{42}$$

$$\begin{aligned}\sigma_{\rm KN,nth} &= \frac{1}{2n_{\rm e,nth}}\int d\gamma_{\rm e}\int d\mu_{\rm e}\frac{dn_{\rm e,nth}}{d\gamma_{\rm e}}\\ &\quad (1-\mu_{\rm e}\sqrt{1-\gamma_{\rm e}^{-2}})\sigma_{\rm KN},\end{aligned} \tag{43}$$

where $dn_{\rm e,th}/d\gamma_{\rm e}$ is the Maxwell–Jüttner distribution function described in Equation (A1), $dn_{\rm e,nth}/d\gamma_{\rm e}$ is the distribution function of a nonthermal electron that is assumed to be isotropic in the momentum space, and $\sigma_{\rm KN}$ is the Klein–Nishina cross section defined in the electron rest frame,

$$\begin{aligned}\sigma_{\rm KN} = \sigma_{\rm T}&\frac{3}{4\epsilon_{\rm e}^2}\\ &\left[2+\frac{\epsilon_{\rm e}^2(1+\epsilon_{\rm e})}{(1+2\epsilon_{\rm e})^2}+\frac{\epsilon_{\rm e}^2-2\epsilon_{\rm e}-2}{2\epsilon_{\rm e}}\ln(1+2\epsilon_{\rm e})\right],\end{aligned} \tag{44}$$

where $\epsilon_{\rm e}$ is the photon energy, which is normalized by the rest-mass energy of electrons, in the electron rest frame.

We tabulate the modified cross section for thermal and nonthermal electrons before the GRRT calculations. It should be noted that the nonthermal electrons are divided into subgroups by their Lorentz factor in the fluid rest frame, which is explained in the next subsection.

5.3.2. Scattering Probability

It should be determined whether the Compton scattering occurs at each full integration time step of the geodesic equation. In order to efficiently calculate the inverse-Compton scatterings in scattering-thin plasmas, it is useful to introduce the the bias parameter b (Dolence et al. 2009),

$$P_{({\rm s})} = 1-\exp\left(-b\Delta\tau_{\nu({\rm s})}\right), \tag{45}$$

where the biased parameter is described in the same manner as in Dolence et al. (2009), i.e., $b = \max(1, \alpha\Theta_{\rm e}^2/\tau_{\rm s\ (max)})$ for thermal plasmas. We basically set $\alpha = \alpha_0/\langle\Theta_{\rm e}\rangle^2$, where $\langle\Theta_{\rm e}\rangle$ is the volume-averaged dimensionless electron temperature, and α_0 is a factor that we set depending on the problems ($\alpha \sim 10^{0-3}$ in this paper). The prescription of b for the scattering includes nonthermal electrons and is explained two paragraphs down.

Due to the introduction of the bias parameter b, each superphoton is split into two superphotons by dividing the weight w, when it is determined to be scattered. The weight of the scattered photons $w_{\rm s}$ and the other one are described as follows:

$$w_{\rm s} = w\left[\frac{1-\exp\left(\Delta\tau_{\nu({\rm s})}\right)}{1-\exp(-b\Delta\tau_{\nu({\rm s})})}\right], \tag{46}$$

$$w_{\rm nos} = w - w_{\rm s} \tag{47}$$

so that the number of photons is conserved via the scattering processes with the split of the superphotons.[5]

When we include the nonthermal electrons, we further extend this method. First, we set the bias parameter b for nonthermal electrons as follows[6]:

$$b_{{\rm nth},i} = b_{\rm th}\frac{\Delta\tau_{\nu({\rm s})\ {\rm th}}}{\Delta\tau_{\nu({\rm s})\ {\rm nth},i}}, \tag{48}$$

where $b_{\rm th}/b_{{\rm nth},i}$ and $\Delta\tau_{\nu({\rm s})\ {\rm th}}/\Delta\tau_{\nu({\rm s})\ {\rm nth},i}$ are the bias parameter and the optical depth for the Compton scattering for thermal/nonthermal electrons, respectively. The subscript i identifies a subgroup of nonthermal electrons, which is introduced to accelerate the calculation. In astrophysical plasmas, nonthermal electrons with a power-law distribution $\gamma_{\rm e}^{-p}$ usually have a

[5] We note that Equation (46) leads to $w_{\rm s} = w/b$ for the limit $\Delta\tau_{\nu({\rm s})} << 1$, which is consistent with Dolence et al. (2009).

[6] For the scatterings in purely nonthermal plasmas, we define $b_{\rm nth,1} = \max(1, 1/\tau_{\rm s\ (max)})$ and replace $b_{\rm th}$ and $\Delta\tau_{\nu({\rm s})\ {\rm th}}$ by $b_{\rm nth,1}$ and $\Delta\tau_{\nu({\rm s})\ {\rm nth},1}$, respectively, for $i \geqslant 2$.

power-law index $p > 0$, i.e., the number density of nonthermal electorns with a high Lorentz factor is very small. Huge computational time is therefore required to sample the nonthermal electrons with a high Lorentz factor with an MC method. In order to avoid this problem, we divide the energy distribution of nonthermal electrons into subgroups with their Lorentz factor.

We summarize our practical method to determine whether the scattering occur at each time step and which of the thermal and nonthermal electrons are sampled if the scattering takes place. We tabulate the modified cross section for each subgroup of the nonthermal electrons,

$$\sigma_{\mathrm{KN,nth},i} = \frac{1}{2n_{\mathrm{e,nth}}} \int_{\gamma_{\mathrm{e,min},i}}^{\gamma_{\mathrm{e,max},i}} d\gamma_{\mathrm{e}} \int_{-1}^{1} d\mu_{\mathrm{e}} \frac{dn_{\mathrm{e,th}}}{d\gamma_{\mathrm{e}}} (1 - \mu_{\mathrm{e}}\sqrt{1 - \gamma_{\mathrm{e}}^{-2}})\sigma_{\mathrm{KN}}, \tag{49}$$

as well as that for thermal electrons (which are not divided into subgroups). Then the optical depth for the Compton scattering is calculated as

$$\Delta\tau_{\nu(\mathrm{s})\ \mathrm{th}} = \left(\frac{\nu_{\mathrm{f}}}{\nu_{\mathrm{z}}}\right) n_{\mathrm{e,th}}\sigma_{\mathrm{KN,th}}\Delta l, \tag{50}$$

$$\Delta\tau_{\nu(\mathrm{s})\ \mathrm{nth},i} = \left(\frac{\nu_{\mathrm{f}}}{\nu_{\mathrm{z}}}\right) n_{\mathrm{e,nth},i}\sigma_{\mathrm{KN,nth},i}\Delta l, \tag{51}$$

The scattering probability is calculated as

$$P_{(\mathrm{s})} = 1 - \exp\left[-\left(b_{\mathrm{th}}\Delta\tau_{\nu(\mathrm{s})\ \mathrm{th}} + \sum_{i=1}^{i_{\mathrm{max}}} b_{\mathrm{nth},i}\Delta\tau_{\nu(\mathrm{s})\ \mathrm{nth}.i}\right)\right]. \tag{52}$$

We generate a pseudo-random number ξ_1 $(0 \leqslant \xi_1 \leqslant 1)$ to determine whether the superphotons are scattered at each time step. If the following condition is satisfied, the superphoton is scattered:

$$P_{(\mathrm{s})} > \xi_1. \tag{53}$$

When this condition is satisfied, we examine which of the thermal and nonthermal electrons scatters the superphoton. We assume that the thermal electrons scatter the superphotons if the following relation is satisfied:

$$\frac{b_{\mathrm{th}}\Delta\tau_{\nu(\mathrm{s})\ \mathrm{th}}}{b_{\mathrm{th}}\Delta\tau_{\nu(\mathrm{s})\ \mathrm{th}} + \sum_{i=1}^{\mathrm{i_{max}}} b_{\mathrm{nth},i}\Delta\tau_{\nu(\mathrm{s})\ \mathrm{nth}.i}} \geqslant \xi_2, \tag{54}$$

where, ξ_2 $(0 \leqslant \xi_2 \leqslant 1)$ is a newly generated random number. The nonthermal electrons in the subgroup $i = i'(< i_{\mathrm{max}})$ are selected when the following condition is satisfied:

$$\frac{b_{\mathrm{th}}\Delta\tau_{\nu(\mathrm{s})\ \mathrm{th}} + \sum_{i=1}^{i'} b_{\mathrm{nth},i}\Delta\tau_{\nu(\mathrm{s})\ \mathrm{nth}.i}}{b_{\mathrm{th}}\Delta\tau_{\nu(\mathrm{s})\ \mathrm{th}} + \sum_{i=1}^{\mathrm{i_{max}}} b_{\mathrm{nth},i}\Delta\tau_{\nu(\mathrm{s})\ \mathrm{nth}.i}} < \xi_2 \leqslant \frac{b_{\mathrm{th}}\Delta\tau_{\nu(\mathrm{s})\ \mathrm{th}} + \sum_{i=1}^{i'+1} b_{\mathrm{nth},i\Delta\tau_{\nu(\mathrm{s})\ \mathrm{nth}.i}}}{b_{\mathrm{th}}\Delta\tau_{\nu(\mathrm{s})\ \mathrm{th}} + \sum_{i=1}^{\mathrm{i_{max}}} b_{\mathrm{nth},i}\Delta\tau_{\nu(\mathrm{s})\ \mathrm{nth}.i}}. \tag{55}$$

In the other case, the nonthermal electrons in the subgroup $i = i_{\mathrm{max}}$ are selected.

5.3.3. Solving the Compton Scattering

When the condition for the scattering is satisfied, we solve the Compton scattering with an MC method. First of all, (i) a scattering electron in the fluid rest frame is sampled, and then, (ii) the four-momentum of the scattered photon is determined using another pseudo-random number.

Before the Compton scattering, the scattering electrons are sampled as follows:

1. The Lorentz factor of thermal or nonthermal electrons in the fluid rest frame is determined. For thermal electrons, the Lorentz factor of the electrons is sampled to reproduce the Maxwell–Jütter distribution (Equation (A1)). We employ a procedure based on the rejection method described in Canfield et al. (1987), which is summarized in Appendix A.2.1. On the other hand, for nonthermal electrons with a single/broken power-law distribution, the Lorentz factor of the scattering electrons can be sampled much easier by the inverse function method descibed in Appendix A.2.2 and A.2.3.
2. The direction of the velocity of the scattering electron, i.e., the angle between the momenta of the scattering electron and the incident photon, is determined. When we sample the scattering electrons, the relativistic motion of the electron should be taken into consideration during the MC sampling. This is because (i) the scattering cross section in the fluid rest frame is $(1 - \mu_{\mathrm{e}}\beta_{\mathrm{e}})\sigma_{\mathrm{KN}}$, and (ii) σ_{KN} is significantly reduced when the Doppler-boosted photon energy in the electron rest frame is significantly higher than the rest-mass energy of electrons (Gorecki & Wilczewski 1984). In order to take into account these effects, we follow the algorithm in Canfield et al. (1987) as follows. The probability distribution function is anisotropic by the factor $(1 - \mu_{\mathrm{e}}\beta_{\mathrm{e}})$. The cosine of the angle between the incident photon and the scattering electron μ_{e} is then sampled by the inverse function method using the pseudo-random number ξ_3 $(0 \leqslant \xi_3 \leqslant 1)$,
$$\mu_{\mathrm{e}} = \frac{1 - \sqrt{1 + \beta_{\mathrm{e}}^2 + 2\beta_{\mathrm{e}} - 4\beta_{\mathrm{e}}\xi_3}}{\beta_{\mathrm{e}}}. \tag{56}$$
There still remains the degree of freedom of the other angle of the four-momentum of the electron, and this angle is sampled by a uniform random number. At this step, the four-momentum of the electron is tentatively determined.
3. Finally, we examine the validity of the sampled electrons with their four-momentum using the rejection method. We accept the sampled electron if it satisfies
$$\frac{\sigma_{\mathrm{KN}}}{\sigma_{\mathrm{T}}} \geqslant \xi_4, \tag{57}$$
where ξ_4 $(0 \leqslant \xi_4 \leqslant 1)$ is a pseudo-random number, and σ_{KN} shown in Equation (44) is evaluated by the photon energy in the electron rest frame ϵ_{e}, which is calculated by the Lorentz transformation of the four-momentum of the incident photon from the fluid rest frame to the electron rest frame of the sampled electron.

Next, we sample the four-momentum of the scattered photons. As described above, the four-momentum vector of the incident photons is Lorentz-transformed from the fluid rest frame to the electron rest frame. Using the pseudo-random

number ξ_5 ($0 \leqslant \xi_5 \leqslant 1$), the tentative value of the scattered photon energy can be represented as

$$\epsilon'_{\rm e} = (1 - \xi_5)\epsilon'_{\rm e,min} + \xi_5 \epsilon'_{\rm e,max}, \tag{58}$$

where $\epsilon'_{\rm e}$ is related to $\epsilon_{\rm e}$ and the cosine of the angle between the electron and the scattered photon $\mu'_{\rm e} = 1 + 1/\epsilon_{\rm e} + 1/\epsilon'_{\rm e}$, so that $\epsilon'_{\rm e,min} = (1 + 2\epsilon_{\rm e})/\epsilon_{\rm e}$ and $\epsilon'_{\rm e,max} = \epsilon_{\rm e}$. Once ϵ_e is determined, we obtain μ'_e. The remaining angle, whose probability distribution function uniformly distributes [0, 2π), is determined by generating another pseudo-random number.

Finally, in order to examine whether the tentative value of $\epsilon'_{\rm e}$ is presumable, we accept the value that satisfies the following relation using the pseudo-random number ξ_6 ($0 \leqslant \xi_6 \leqslant 1$)

$$\frac{d\sigma_{\rm KN}/d\epsilon'_{\rm e}}{\max(d\sigma_{\rm KN}/d\epsilon'_{\rm e})} \geqslant \xi_6, \tag{59}$$

where

$$\frac{d\sigma_{\rm KN}}{d\epsilon'_{\rm e}} = \frac{3\sigma_{\rm T}}{8}\frac{1}{\epsilon_{\rm e}^2}\left(\frac{\epsilon_{\rm e}}{\epsilon'_{\rm e}} + \frac{\epsilon'_{\rm e}}{\epsilon_{\rm e}} - 1 + \mu'^2_{\rm e}\right), \tag{60}$$

$$\max\left(\frac{d\sigma_{\rm KN}}{d\epsilon'_{\rm e}}\right) = \left.\frac{d\sigma_{\rm KN}}{d\epsilon'_{\rm e}}\right|_{\epsilon'_{\rm e}=\epsilon_{\rm e}} = \frac{3\sigma_{\rm T}}{4}\frac{1}{\epsilon_{\rm e}^2}. \tag{61}$$

If the tentative $\epsilon'_{\rm e}$ is rejected, the procedure for sampling the scattered photon is repeated until it is accepted through the rejection method. Once the sampled scattered photon is accepted, the four-momentum of the scattered photon in the electron rest frame is converted into that in the fluid rest frame and in the ZAMO frame via the Lorentz transformation. The covariant four-momentum of photon in the BL frame is also calculated via the coordinate transformation in order to solve the geodesic equations at the next time step.

5.4. Calculation of SED

The SED is calculated after the superphoton escape to the outer boundary of the computational domain. We divide the bins of the photon-frequency in the observer frame ν and the viewing angle $\theta_{\rm ob}$ in such a way that $\Delta \ln \nu$ and $\Delta \cos\theta_{\rm ob}$ are constant. Here viewing angle $\theta_{\rm ob}$ is defined as the angle between the rotation axis of the Kerr BH and the line of sight of observers.

For an observer at the jth viewing angle bin, the value of νL_ν at ith frequency bin can be calculated as follows:

$$\nu L_\nu(i, j) = \frac{4\pi}{\Delta \ln \nu \Delta\Omega \Delta t}\sum_{\rm n} w_{\rm n}(i, j) h\nu_n(i, j), \tag{62}$$

where $w_n(i, j)$ is the weight of nth photons leaving the computational domain from the outer boundary with belonging to the ith frequency bin and the jth viewing-angle bin. We set $\Delta\Omega = 2\pi\Delta\cos\theta_{\rm ob}$ and $\Delta t = 1$ by default.

5.5. Imaging with the Emitter-to-observer MC Algorithm

With the emitter-to-observer MC algorithm, we can also calculate the images of high-energy photons generated via including the Compton and inverse-Compton scatterings. Since the emitter-to-observer MC algorithm traces superphotons approaching the observer in arbitrary directions (the viewing angle between the line of sight and the polar axis $\theta_{\rm ob}$ and x-axis in the equatorial plane $\varphi_{\rm ob}$, respectively), we can simultaneously set a number of observer screens at infinity in the θ and ϕ direction of the computational domain. When we set $N_{\theta\rm (screen)}$ and $N_{\varphi\rm (screen)}$ of the observer screens in the θ and φ direction, the interval of each observer screen is $\Delta\cos\theta = 2/N_{\theta\rm (screen)}$ and $\Delta\varphi = 2\pi/N_{\rm (screen)}$. The solid angles between the neighborhood screens are constant.

When a superphoton approaches the outer boundary of the computational domain of the GRRT calculations, we evaluate $\theta_{\rm ob}$ and $\varphi_{\rm ob}$ using the final position and the four-momentum of the superphoton. Then, the corresponding observer screen for the superphoton is determined from $N_{\theta\rm (screen)} \times N_{\varphi\rm (screen)}$ of the screen.[7]

Next, a pixel of the screen at which the superphotons are detected at infinity, can be calculated with the four-momentum of the superphoton, as is the case for the screen of the observer-to-emitter RT algorithm. Namely, the coordinates of the observer screen where the superphoton penetrates, x (horizontal direction) and y (vertical direction) in the unit of $r_{\rm g}$, can be described as

$$(x, y) = \left(\frac{p_\varphi}{p_t}\frac{1}{\sin\theta_{\rm ob}}, -\frac{p_\theta}{p_t}\right). \tag{63}$$

We note that p_t, p_θ, and p_φ are the four-momentum of the superphotons in the Boyer–Lindquist coordinate at the outer boundary of the computational domain. When the coordinate (x, y) is evaluated, the corresponding pixel can be directly determined.

Finally, the intensity at the pixel is computed as follows:

$$I_\nu(i, j, k) = \frac{1}{\nu(i)\Delta \ln \nu \Delta\Omega\Delta A\Delta t}\sum_n w_n(i, j, k) {\rm h}\nu(i, j, k), \tag{64}$$

where $I_\nu(i, j, k)$ and $w_n(i, j, k)$ are the intensity and the weight of superphotons in the ith photon-frequency bin, the jth pixel in the x direction, and the kth pixcel in the y direction of the screen. We note $\Delta\Omega = \Delta\cos\theta\Delta\varphi = 4\pi/N_{\theta\rm (screen)}N_{\rm (screen)}$, and $\Delta A = \Delta x_{\rm pixel}\Delta y_{\rm pixel}$, where $\Delta x_{\rm pixel}$ and $\Delta y_{\rm pixel}$ are the pixel size of the observer screen in the x and y direction, respectively. The width of the photon-frequency bin of the screen is $\Delta \ln \nu$. We set $N_{\varphi\rm (screen)}$=1 to save computational cost in this paper and set $\Delta t = 1$.

6. Numerical Tests

6.1. Trajectory of the Photon

We test the geodesics solver by comparing the numerical results and the analytic solution on the equatorial plane of a Kerr BH for the case with $p_\varphi = -ap_t$ (Chandrasekhar 1983),

$$\varphi = \frac{a}{r_+ - r_-}\left[\ln\left(\frac{r}{r_+} - 1\right) - \ln\left(\frac{r}{r_-} - 1\right)\right], \tag{65}$$

where r_+ and r_- are the outer and inner horizon of the Kerr BHs $r_\pm = M \pm \sqrt{M^2 - a^2}$.

[7] Although the module computing $\varphi_{\rm ob}$-dependent images is implemented, we only demonstrate the $\varphi_{\rm ob}$-averaged images (i.e., $\Delta\varphi_{\rm ob} = 2\pi$) for the computation using the emitter-to-observer MC algorithm throughout this paper to save computational cost. We note that for the computation using the observer-to-emitter RT algorithm, the $\varphi_{\rm ob}$-dependent images are presented.

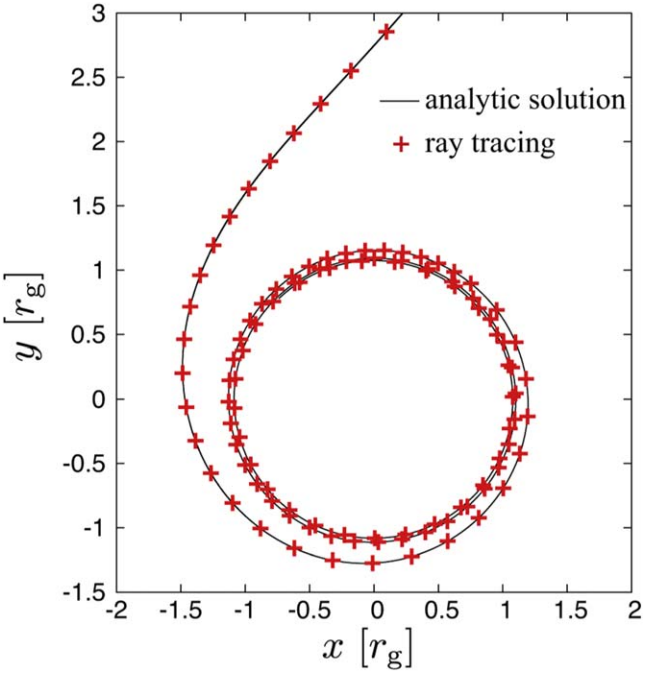

Figure 1. Comparison between the ray-tracing calculation (red points) and the analytic solution (black line) of the trajectory of a photon on the equatorial plane of a Kerr BH with $a_* = 0.998$.

Figure 1 shows the result for $a_* = 0.998$, where $a_* \equiv a/M$. The BH rotates in the counterclockwise direction. The photons are initiated at $r = 10r_g$, $\theta = \pi/2$, and φ is given by Equation (65). The four-momentum of photon is $p_t = -E$, $p_\theta = 0$, $p_\varphi = a_* E$, and p_r is derived from the the constraint $p^\mu p_\mu = 0$. As the photon approaches the BH, its trajectory is strongly affected by the BH gravity and the frame-dragging effect. The result computed by our code (red points) reproduces the analytic solution well (black line).

6.2. Black Hole Shadow

As another tests of the geodesic equation solver, the shape of the BH shadows is calculated with viewing angles of 30° and 90° for $a_* = 0$, 0.5, and 0.998, and it is shown in Figure 2. The photon trajectory is solved from the observer screen with the time-reversing way. The region in which the photon is captured by the BH is shown in black, while light gray represents the area in which the photons escape to infinity. The dotted orange lines represent the shape of the BH shadow given by the analytic solution, whose radius and angle in the observer screen is described as follows (Bardeen 1973; Johannsen 2013; Wong 2021):

$$x = -\frac{\xi}{\sin\theta_{\rm ob}}, \tag{66}$$

$$y = \pm\sqrt{\eta + a^2\cos^2\theta_{\rm ob} - \xi^2\cot^2\theta_{\rm ob}}, \tag{67}$$

where x and y are the Cartesian coordinates on the observer screen in which the BH spin vector projected onto the screen is on the y-axis, and $\theta_{\rm ob}$ is the viewing angle of the observer. The variables ξ and η are parameterized by the radius of the corresponding photon orbit $r_{\rm ph}$ as follows:

$$\xi = -\frac{r_{\rm ph}^2(r_{\rm ph} - 3M) + a^2(r_{\rm ph} + M)}{a(r_{\rm ph} - M)}, \tag{68}$$

$$\eta = \frac{r_{\rm ph}^3[4a^2M - r_{\rm ph}(r_{\rm ph} - 3M)^2]}{a^2(r_{\rm ph} - M)^2} \tag{69}$$

We note that $r_{\rm ph}$ continuously exists between their minimum and maximum values $r_{\rm ph,min}$ and $r_{\rm ph,max}$, which are the roots of the equation

$$\begin{aligned} y^2 = a^2\cos^2\theta_{\rm ob} + \frac{1}{a^2(r_{\rm ph} - M)^2} \\ [a^2(r_{\rm ph} + M) + r_{\rm ph}^2(r_{\rm ph} - 3M)]^2\cot^2\theta_{\rm ob} \\ + r_{\rm ph}^3[r_{\rm ph}(r_{\rm ph} - 3M)^2 - 4a^2] = 0, \end{aligned} \tag{70}$$

where the region formed by these unstable circular photon orbits is the so-called photon shell (Event Horizon Telescope Collaboration 2019e; Johnson et al. 2020; Kawashima et al. 2021).

Our numerical calculations successfully reproduce the analytical shape of the BH shadow for the various inclination angles and BH spin. We note that as the BH spin increases, the location of the BH shadow shifts in the direction perpendicular to the BH spin vector projected onto the observer screen because of the frame-dragging effect (for the application to a possible estimate of the BH spin, see Kawashima et al. 2019; Chael et al. 2021).

More tests of computations of geodesic equations and BH shadows using `RAIKOU` are also carried out with the GRRT code comparison projects of the EHT (Gold et al. 2020).

6.3. Compton Scattering Via Thermal Electrons

In this section, we test the Compton scattering of blackbody photons via thermal electrons in a uniform plasma sphere. For the sake of the simplicity, the spacetime is assumed to be flat (i.e., the Minkowski spacetime) and the absorption processes are ignored here. The radiative temperature of blackbody photons $T_{\rm rad}$ is set to be $k_{\rm B}T_{\rm rad}/m_{\rm e}c^2 = 10^{-8}$, where $k_{\rm B}$, $m_{\rm e}$, and c are the Boltzmann constant, electron rest mass, and speed of light, respectively. The blackbody photons are injected from the inner sphere at $r = r_{\rm in} = 1$ cm. The outer boundary of the computational domain is located at $r = r_{\rm out} = 10^5$ cm, so that the finite radius of $r_{\rm in}$ affect the results only negligibly.

We examine the Compton scattering via thermal electrons as in Dolence et al. (2009). The temperature and number density of electrons are set to be $\Theta_{\rm e} = k_{\rm B}T_{\rm e}/m_{\rm e}c^2 = 4$ and $n_{\rm e,th} = \tau_{\rm (s)}/\sigma_{\rm T}(r_{\rm out} - r_{\rm in})$, respectively. Here, $\tau_{\rm (s)}$ is the optical depth for the Thomson scattering, and we set $\tau_{\rm (s)} = 10^{-4}$, 10^{-1}, and 3. Figure 3 displays the resulting SEDs, which reproduce the results shown in Dolence et al. (2009).

In Figure 3, the SEDs are also decomposed into the SEDs of photons without being scattered, with being scattered once, twice, and three or more times. The optically thin cases (i.e., $\tau_{(s)} = 10^{-4}$ and 10^{-1}) more clearly show the feature of individual Comptonization processes. Spectral bumps at $\nu \sim 10^{15}$, 10^{17}, and $\sim 10^{19}$ Hz are formed via inverse-Compton scattering, which is consistent with the fact that the change in photon frequency per scattering $\Delta\nu$ is $\Delta\nu/\nu \sim 16\Theta_{\rm e}^2 \sim 10^2$ (e.g., Rybicki & Lightman 1979). One can also find that the L_ν

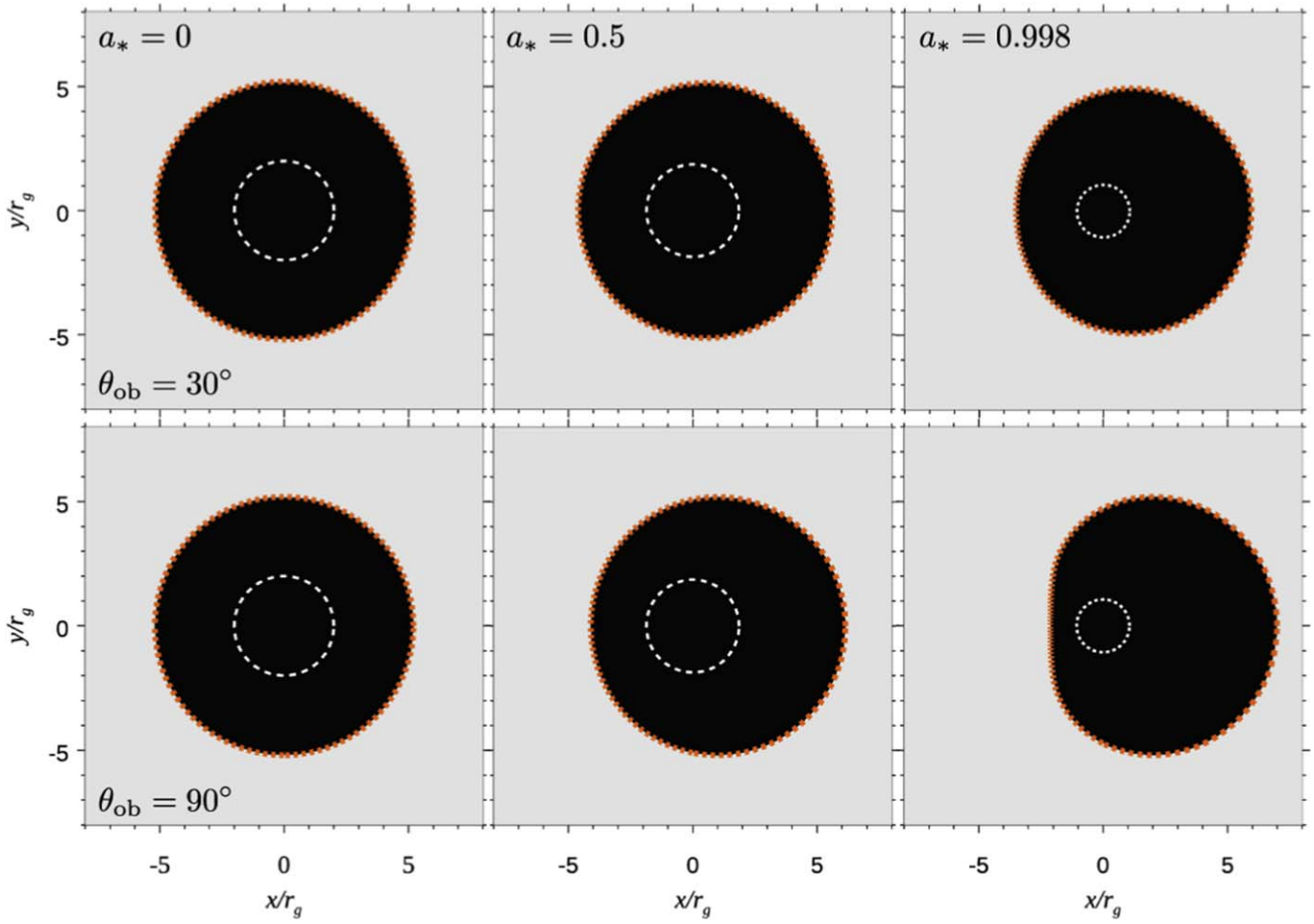

Figure 2. The computed BH shadows for the case with $a_* = 0$ (left), 0.5 (center), and 0.998 (right). The top and bottom panels display the images with viewing angles $\theta_{\rm ob} = 30°$ and 90°, respectively. The region in which the photon emitted from the observer screen with the time-reversing way is captured by the BH is shown in black, while light gray represents the area in which the photons escape to infinity. The dotted orange lines are the edge of BH shadow obtained by the analytic solution. The dashed white lines represent the radius of the outer horizon of the BHs in BL coordinates.

at each spectral bump is reduced by $\sim 10^{-4}$ and $\sim 10^{-1}$ for the case with $\tau_{(\rm s)} = 10^{-4}$ and 10^{-1}, respectively, since L_ν at the frequency of the scattered photon is reduced by the scattaring probability $1 - \exp(-\tau_{(\rm s)}) \sim \tau_{(\rm s)}$ in the optically thin limit. In the optically thick case $\tau_{(\rm s)} = 3$, the number of scatterings is ~ 10 and the Compton y-parameter is significantly greater than unity $y = 16\Theta_{\rm e}^2 \max(\tau_{(\rm s)}, \tau_{(\rm s)}^2) \sim 2 \times 10^3 \gg 1$, which results in the formation of the Wien-like peak around $3k_{\rm B}T_{\rm e}/h \sim 10^{21}$ Hz. The resulting SEDs therefore reproduce the spectral features of Comptonization well in opticallty thin and thick plasmas.

Figure 4 shows a self-convergence test of the SEDs of thermal Comptonization of the incident blackbody photons. The SEDs in Figure 3, where the number of superphotons $N = 1.28 \times 10^8$ and $=3.84 \times 10^8$ are used for the optically thin ($\tau_{(\rm s)} = 10^{-4}$ and 10^{-1}) and thick ($\tau_{(\rm s)} = 3$) plasma sphere models, respectively, are employed as references. One may find that the integral fractional error decreases following $N^{-1/2}$, as expected. The superphotons are generated on the surface of the inner boundary at $r = 1$ cm in such a way that the number of the superphotons generated in each mesh is uniform, where the computational domain is divided into $N_\theta = 16$ and $N_\varphi = 1$ in θ and φ directions, respectively, and the mesh size is $\Delta \cos\theta = 2/N_\theta$ and $\Delta\varphi = 1$. Inside each mesh, the superphotons are uniformly distributed in space on the surface with a pseudo-random number. For the Compton scatterings, we set $\alpha_0 = 2$ for the biased parameter b. The computational cost for the reference models is $\sim$2.4, 2.3, and 1.3 node hours for $\tau_{(\rm s)} = 10^{-4}$, 10^{-1}, and 3, respectively. Here, the computations are carried out on a Cray XC50 system, where two Intel Xeon Skylakes 6148 (20 cores, 2.4 GHz, 1.536 TFlops) are implemented per node, throughout this paper.

6.4. Compton Scattering Via Nonthermal Electrons

We examine the Comptonization of blackbody photons via nonthermal electrons with single and broken power-law distribution functions in the uniform spherical plasma. The radial optical depth against the Thomson scattering is 10^{-4}. In this subsection, we show the SEDs of νL_ν rather than L_ν to clearly present the high-energy photons that are Compton-upscattered by electrons with a high Lorentz factor.

Figure 5 displays the SEDs of photons that are Comptonized via nonthermal electrons with a single power-law distribution $n_{\rm e,nth} \propto \gamma_{\rm e}^{-p}$ for $\gamma_{\rm e,min} \leqslant \gamma_{\rm e} \leqslant \gamma_{\rm e,max}$, where $\gamma_{\rm min} = 2$ and $\gamma_{\rm max} = 2 \times 10^4$. The SED peak of the photons that experienced one-scattering event appears at $\sim 10^{21}$ Hz. This peak is formed by inverse-Compton scattering with electrons whose Lorentz factor $\gamma_e \simeq \gamma_{\rm e,max}$, i.e., the photons with a peak frequency of the injected blackbody photons of $\nu_{\rm bb} \simeq 4 \times 10^{12}$

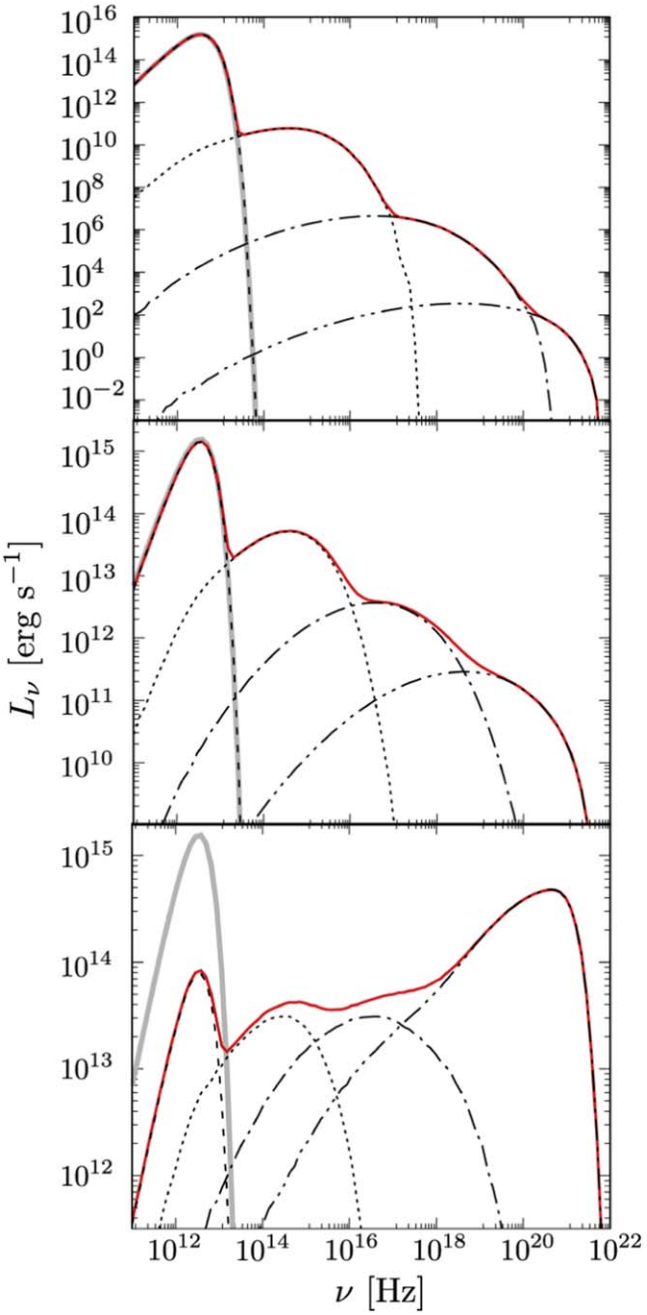

Figure 3. Comptonized SEDs of blackbody photons, which are scattered by the hot electrons $\Theta_e = 4$ in the plasma sphere with an optical depth for the Thomson scattering of $\tau_{(s)} = 10^{-4}$ (top), 10^{-1} (middle), and 3 (bottom). The emitter-to-observer MC algorithm is used. The resulting SEDs are displayed with solid red lines. Black lines represent the decomposed SEDs, whose photons escaped toward the observer without being scattered (dashed), with being scattered once (dotted), twice (dash–dotted-dash), and more than three times (dash–dot-dot–dashed). The solid gray lines depict the incident blackbody spectra, which overlap the spectra of unscattered photons (i.e., dashed lines), except in the case with $\tau_{(s)}$=3. The width of the photon-frequency bin is $\Delta \log \nu = 0.12$.

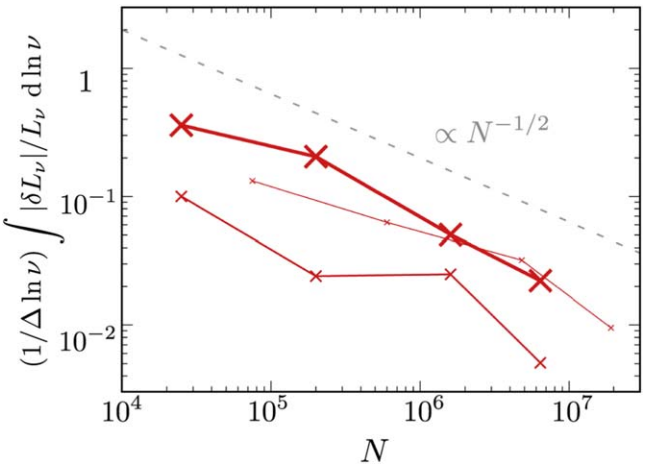

Figure 4. Self-convergence test of the Comptonized SEDs shown in Figure 3. The integral fractional error as a function of the number of generated superphotons N is shown as thick red ($\tau_{(s)} = 10^{-4}$), moderate red ($\tau_{(s)} = 10^{-1}$), and thin red ($\tau_{(s)} = 3$) lines. The dashed gray line indicates the error proportional to $N^{-1/2}$ as reference.

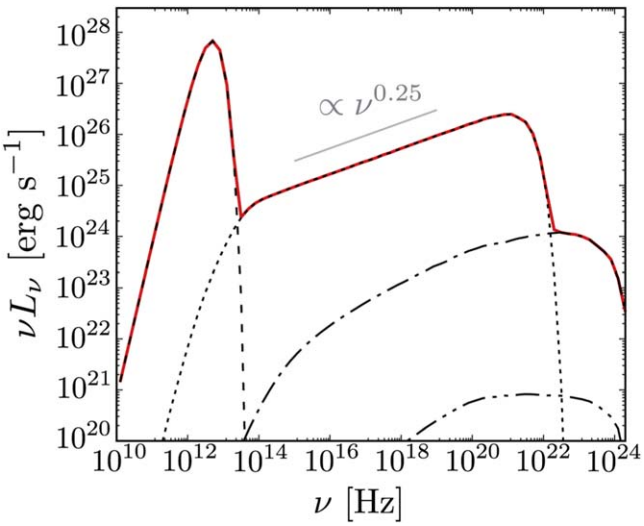

Figure 5. Comptonized SEDs of blackbody photons that are scattered by nonthermal electrons with a power-law index p=2.5 in the plasma sphere. The minimum and maximum Lorentz factors of the nonthermal electrons are $\gamma_{e,min} = 2$ and $\gamma_{e,max} = 2 \times 10^4$, respectively. The optical depth for the Thomson scattering is $\tau_{(s)} = 10^{-4}$. The resulting SEDs are displayed with solid red lines. The black lines represent the decomposed SEDs, whose photons escaped toward the observer without being scattered (dashed), with being scattered once (dotted), twice (dash–dot-dashed), and more than three times (dash–dot-dot–dashed). The emitter-to-observer MC algorithm is used. The width of the photon-frequency bin is $\Delta \log \nu = 0.2$.

Hz are upscattered to the photon frequency $\gamma^2_{e,max}\,\nu_{bb} \simeq 10^{21}$ Hz. The additional peak at $\nu \sim 10^{23}$ Hz is formed by two-scattering events, where the peak frequency appears at $\lesssim \gamma_{e,max} m_e c^2/h \sim 10^{24}$ Hz because the scattering cross section is smaller (i.e., Klein–Nishina effect).

Figure 6 shows the Comptonized SEDs with the same model setup, except that the maximum Lorentz factor of the nonthermal electrons is higher, $\gamma_{e,max} = 2 \times 10^6$. In the gamma-ray energy bands, only one remarkable spectral peak appears at $\nu \sim 10^{25}$ Hz, although two peaks appear in the gamma-ray energy band for the model with the lower maximum Lorentz factor (see Figure 5). This is because the spectral peak formed by the one-scattering component $\gamma^2_{e,max}\,\nu_{bb} \sim 10^{25}$ Hz is similar to the possible maximum peak of Comptonized SEDs $\gamma_{e,max} m_e c^2/h \sim 10^{26}$ Hz. For the component with twice or more scattering, the Compton scattering with a high Lorentz factor of the electrons is highly suppressed by the Klein–Nishina effect, and the spectral peak appears at $\nu \lesssim \gamma_{e,max} m_e c^2/h \sim 10^{26}$ Hz.

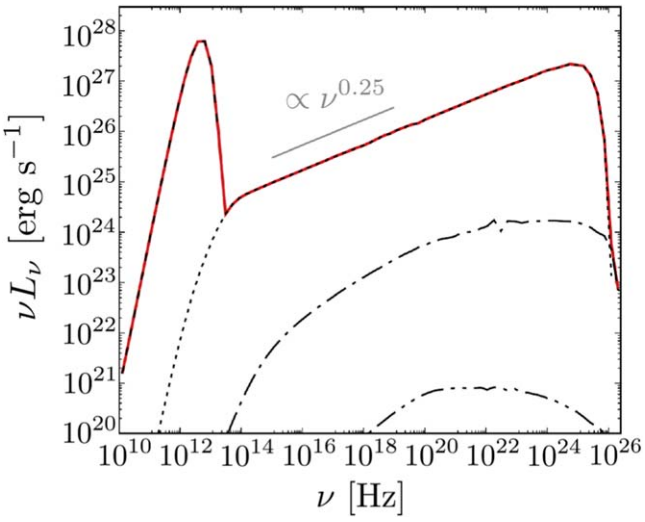

Figure 6. The same as Figure 5, except that $\gamma_{\rm max} = 2 \times 10^6$.

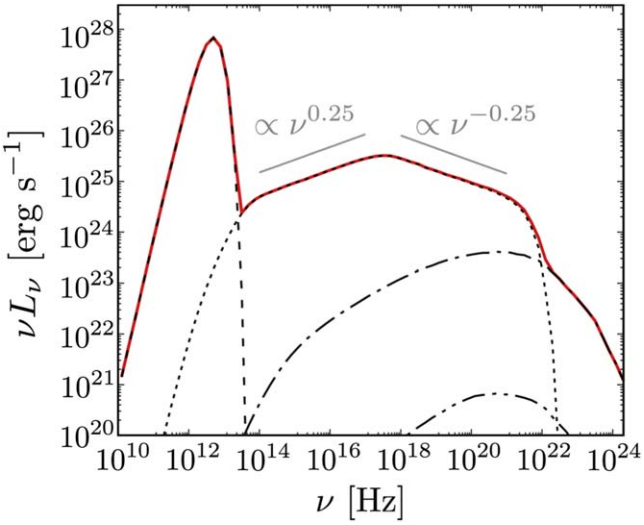

Figure 7. The same as Figure 5, but for the broken power-law distribution of nonthermal electrons. The power-law indices are $p_1 = 2.5$ and $p_2 = 3.5$ between $2 \leqslant \gamma_{\rm e} \leqslant 2 \times 10^2$ and $200 < \gamma_{\rm e} \leqslant 2 \times 10^4$, respectively.

In Figure 7, we show the result of Comptonized SEDs that were calculated for a broken power-law model of nonthermal electrons. The power-law distribution extends from $\gamma_{\rm e,min} = 2 \times 10^2$ to $\gamma_{\rm e,max} = 2 \times 10^4$, and the power-law index is broken at $\gamma_{\rm br} = 2 \times 10^2$. The power-law indices are $p_1 = 2.5$ and $p_2 = 3.5$ in $\gamma_{\rm e,min} \leqslant \gamma_{\rm e} \leqslant \gamma_{\rm e,br}$ and $\gamma_{\rm e,br} < \gamma_{\rm e} \leqslant \gamma_{\rm e,max}$, respectively. As a consequence of the break in the power-law electron distribution function, the power-law SED of the photons also breaks at $\nu_{\rm br} \sim (4k_{\rm B}T_{\rm e}/h)\gamma_{\rm br}^2 \sim 10^{17}$ Hz. The power-law indices in the SED are $(3 - p_1)/2 = 0.25$ and $(3 - p_2)/2 = -0.25$ below and above $\nu_{\rm br}$, respectively.

Figure 8 shows a self-convergence test of the SEDs of the nonthermal Comptonization of the incident blackbody photons shown in Figures 5–7. The SEDs in Figures 5, 6, and 7, where the number of superphotons $N \simeq 1.6 \times 10^8$, $\simeq 8.2 \times 10^8$, and $N \simeq 3.2 \times 10^8$ are used, respectively, are employed as references. The superphotons are generated in the same manner as in the previous section. To calculate the biased parameter $b_{{\rm nth},i}$, we divide the nonthermal electrons into two subgroups. The

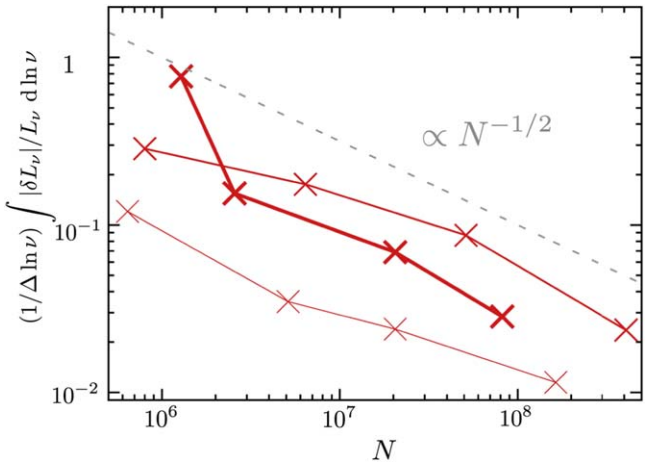

Figure 8. The same as Figure 4, except that the self-convergence is examined for the SEDs shown in Figures 5–7, which are Comptonized by nonthermal electrons. The thick, moderate, and thin red lines represent the integral fractional error of the SEDs that are Comptonized by the nonthermal electrons shown in Figure 5 (single power law $p = 2.5$, $\gamma_{\rm e,min} = 2$, $\gamma_{\rm e,max} = 2 \times 10^4$), Figure 6 (single power law $p = 2.5$, $\gamma_{\rm e,min} = 2$, $\gamma_{\rm e,max} = 2 \times 10^6$), Figure 7 (broken power law $p_1 = 2.5$, $p_2 = 3.5$, $\gamma_{\rm e,min} = 2$, $\gamma_{\rm e,br} = 2 \times 10^2$, $\gamma_{\rm e,max} = 2 \times 10^4$), respectively.

computational cost for the reference models is ∼72.5 (single power law), 280 (single power law with a higher maximum Lorentz factor), and 350 node hours (broken power law). The relative errors accumulated over the photon-frequency bins decrease roughly as $N^{-1/2}$, i.e., the resultant SEDs converge as expected.

6.5. Compton Scattering Via Thermal and Nonthermal Electrons

The top panel of Figure 9 demonstrates the SEDs of blackbody photons that are Comptonized by thermal and nonthermal electrons and its self-convergence test. The calculation setup is the same as that for the SEDs that are Comptonized via thermal electrons and nonthermal electrons with $\tau_{\rm (s)} = 10^4$ shown in Figure 3 , except that the nonthermal electrons with the single power-law distribution of the power-law index p=2.5, $\gamma_{\rm min} = 2$ and $\gamma_{\rm min} = 2 \times 10^6$ with $\tau_{\rm (s)} = 10^4$ is also added (i.e., the total scattering depth of thermal plus nonthermal electrons is $\tau_{\rm (s)} = 2 \times 10^4$). The spectral bump at $\nu \sim 10^{15}$ Hz and the power-law shaped SED in $\nu \gtrsim 10^{16}$ Hz are formed via thermal and nonthermal inverse-Compton scattering, respectively. These spectral features are the same as those for pure thermal and nonthermal inverse-Compton scattering, as shown in Figures 3 and 6.

The bottom panel of Figure 9 shows the result of the self-convergence check. The number of superphotons of the reference SED is $N \simeq 7.7 \times 10^6$. The relative errors accumulated over the photon-frequency bins decrease roughly as $N^{-1/2}$, as expected. The superphotons are generated in the same manner as in the previous section. For the Compton scatterings, we set $\alpha_0 = 4$ to evaluate the biased parameter of the thermal electron scatterings $b_{\rm th}$, and nonthermal biased parameter $b_{{\rm nth},i}$ is evaluated by dividing the nonthermal electrons into three subgroups. The biased parameter is set for these models. The computational cost for the reference models is ∼72.5 node hours.

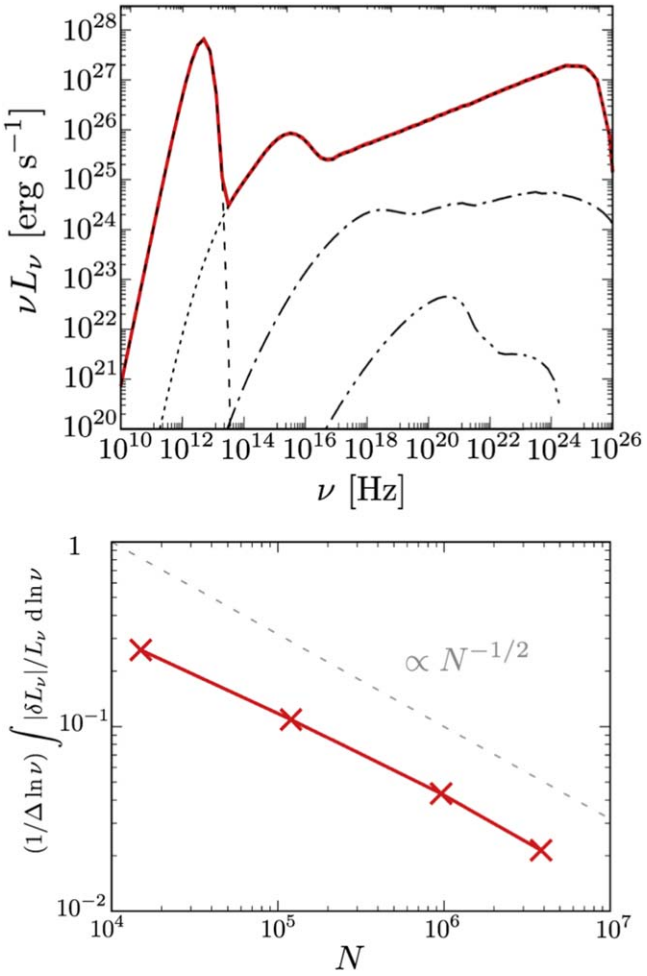

Figure 9. (Top) Comptonized SEDs of blackbody photons scattered by thermal and nonthermal electrons. The optical depths for the Thomson scattering for thermal and nonthermal electrons are set to be the same, i.e., $\tau_{(s)} = 10^{-4}$, respectively. The distribution function of thermal and nonthermal electrons is the same as in Figures 3 and 6, respectively. The width of the photon-frequency bin is $\Delta \log \nu = 0.2$. (Bottom) Integral fractional error of the SED.

6.6. Synchrotron Self-Compton

In this subsection, the synchrotron self-Compton (SSC) processes via nonthermal electrons are tested. We set a plasma sphere with a uniform spatial distribution of the number density of nonthermal electrons $n_{\rm e,nth} = 10^3 {\rm cm}^{-3}$ and a magnetic field strength $B = 10^{-2}$ G, where the orientation of the magnetic field is isotropic. The radius of the plasma sphere is set to be 10^{15} cm. The bulk speed of the plasma sphere is assumed to be zero. We examine the models with a single and broken power-law distribution function of the nonthermal electrons.

First, we present the results for the model with a single power-law distribution of electrons, where the distribution function is shown in Equation (A2). The power-law index is $p = 2.5$ for a Lorentz factor of the nonthermal electrons $\gamma_{\rm e,min} \leqslant \gamma_{\rm e} \leqslant \gamma_{\rm e,max}$, where $\gamma_{\rm e,min} = 10^2$ and $\gamma_{\rm e,max} = 10^7$. Figure 10 shows the resulting SED calculated by `RAIKOU` (red line). As a reference, the SED calculated by a numerical code that is not based on MC methods (`AGN SED tool`; Massaro et al. 2006; Tramacere et al. 2009, 2011), in which one-zone models are assumed, is also plotted as filled black circles. It is found that our result agrees well with the reference.

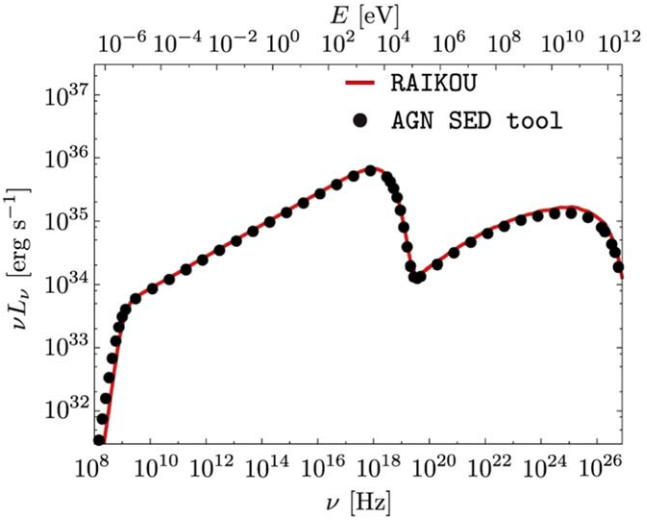

Figure 10. SEDs of SSC via nonthermal electrons with a single power-law distribution. The power-law index is p=2.5 for electrons with a Lorentz factor $\gamma_{\rm e,min} \leqslant \gamma_{\rm e} \leqslant \gamma_{\rm e,max}$, where $\gamma_{\rm e,min} = 10^2$ and $\gamma_{\rm e,max} = 10^7$. The width of the photon-frequency bin is $\Delta \log \nu = 0.2$. The red line and the black circles present the results obtained by `RAIKOU` with the emitter-to-observer MC algorithm and the public code `AGN SED tool`, respectively.

The spectral features in Figure 10 are briefly mentioned here. The SED is steep in $\nu \lesssim 10^9$ Hz because of the synchrotron self-absorbed process. At $10^9 \lesssim \nu \lesssim 10^{17.5}$ Hz, the SED formed by the optically thin synchrotron emission via the nonthermal electrons with $p = 2.5$, i.e., $\nu L_\nu \propto (3-p)/2 = 0.25$ appears. As is well known, the SEDs due to the synchrotron emission via electrons with a power-law distribution is the same as SEDs that are due to the inverse-Compton scattering of photons via nonthermal electrons with the same distribution function (e.g., Rybicki & Lightman 1979). At $\nu \gtrsim 10^{19}$ Hz, the spectral bump caused by the inverse-Compton scattering of the synchrotron photons via nonthermal electrons (i.e., SSC) appears. Here, it should be noted that the SED that formed through the SSC processes shows a bump rather than the simple power-law shape, because the seed photons (i.e., synchrotron photons) have the broadband SEDs, which consequently result in the deviation from the simple power-law SED of the Comptonized photons.

Next, we present the results for the model with a broken power-law distribution of the electrons, where the distribution function is shown in Equations (A4) and (A5). The power-law indices are $p_1 = 1.5$ and $p_2 = 3.5$ for $\gamma_{\rm e,min} \leqslant \gamma_{\rm e} \leqslant \gamma_{\rm e,br}$ and $\gamma_{\rm e,br} \leqslant \gamma_{\rm e} \leqslant \gamma_{\rm e,max}$, respectively, where $\gamma_{\rm e,min} = 10^2$, $\gamma_{\rm e,br} = 10^4$, and $\gamma_{\rm e,max} = 10^7$. Figure 11 shows the resulting SED. As is the calculation with the single power-law model, our computed SED reproduces the SED calculated by the `AGN SED tool` well. Here, we briefly note the spectral features of the calculated SED in Figure 11. As in the single power-law model, the SED is steep at $\lesssim 10^9$ Hz because of the synchrotron self-absorbed process. At $10^9 \lesssim \nu \lesssim 10^{12.5}$ Hz and $10^{12.5} \lesssim \nu \lesssim 10^{17}$ Hz, the optically thin synchrotron emission via nonthermal electrons with p_1 and p_2 appears, respectively. The spectral indices of νL_ν are $(3-p_1)/2 = 0.75$ and $(3-p_2)/2 = -0.25$, respectively. At $\nu \gtrsim 10^{17}$ Hz, the spectral bump caused by the SSC via the nonthermal electrons appears.

Figure 12 displays the self-convergence check of the SEDs of SSC via the single and broken power-law models. As references, we employed the SEDs of SSC shown in Figures 10

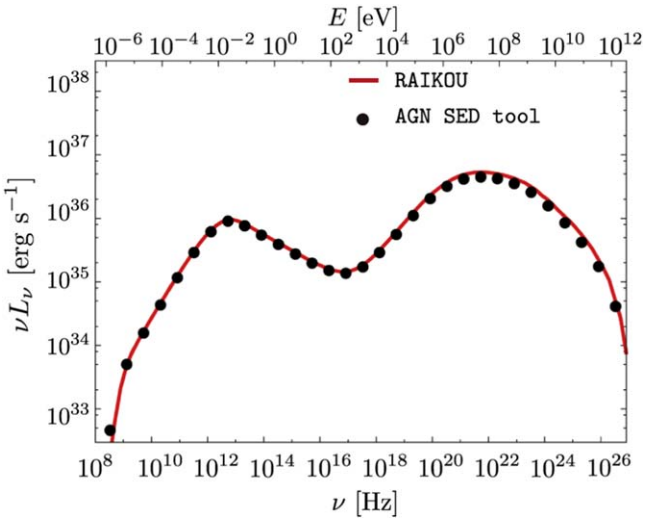

Figure 11. Same as Figure 10, but for the broken power-law distribution. The power-law indices are $p_1 = 1.5$ and $p_2 = 3.5$ for the electrons with a Lorentz factor $\gamma_{e,min} \leqslant \gamma_e \leqslant \gamma_{e,br}$ and $\gamma_{e,br} < \gamma_e \leqslant \gamma_{e,max}$, respectively. Here, we set $\gamma_{e,min} = 10^2$, $\gamma_{e,br} = 10^4$, and $\gamma_{e,max} = 10^7$.

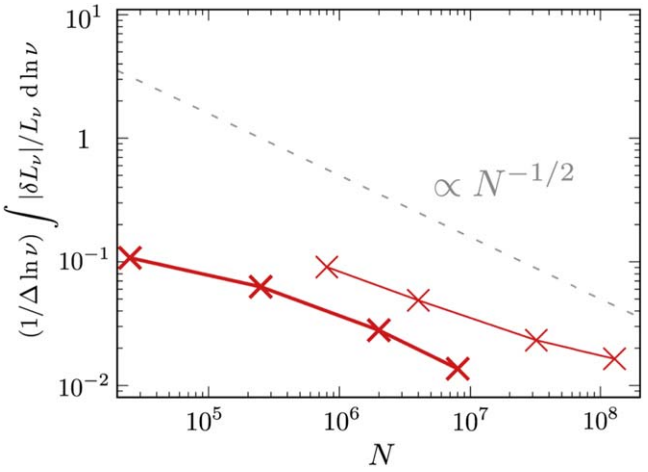

Figure 12. Same as Figure 8, but for the SEDs of the SSC via nonthermal electrons with a single power-law distribution (thick red line) and the broken power-law distribution (thin red line), which are shown in Figures 10 and 11, respectively.

and 11, whose numbers of superphotons are $N = 2.56 \times 10^8$. The superphotons are uniformly generated inside the plasma sphere in such a way that the number of the superphotons that is generated in each volume mesh is uniform, where the number of the meshes is $N_r \times N_\theta \times N_\varphi = 1600 \times 16 \times 1$. Here, the photons are generated in volume rather than in the inner boundary surface for these SSC computations. We note that the meshes are divided linearly in the r direction. Inside each volume mesh, the superphotons are uniformly distributed in space. To calculate the biased parameter $b_{nth,i}$, we divide the nonthermal electrons into three subgroups. The computational cost for the reference models is ~1.2 (single power law) and 12 node hours (broken power law). As expected, the integrated fractional errors decrease roughly as $N^{-1/2}$. We note that the errors are larger in the broken power-law model than in the single power-law model because the number of high-energy electrons is small, so that the resultant fluctuation in the high-energy gamma-ray SED is large in the former model.

6.7. Convergence Check of Emission and Absorption Processes with a Toy Accretion Flow Model

We test the convergence of the SEDs and images of the accretion flow calculated by using the emitter-to-observer MC algorithm. For the tests in this subsection, the Keplerian shell model (e.g., Falcke et al. 2000; Broderick & Loeb 2006; Pu et al. 2016a; Kawashima et al. 2019; Cho et al. 2022), which is a toy model of the RIAFs, is used to set the spatial distribution of MHD plasma around a BH. The BH is assumed to be a Schwarzchild BH with $4.1 \times 10^6 M_\odot$. The spatial distributions of the thermal electrons, nonthermal electrons, electron temperature, and magnetic energy density are set as follows:

$$n_e = 6 \times 10^7 (r/r_g)^{-1.1} \exp(-z^2/2H^2)\ [\mathrm{cm}^{-3}], \quad (71)$$

$$n_{e,nth} = 2.5 \times 10^5 (r/r_g)^{-1.75} \exp(-z^2/2H^2)\ [\mathrm{cm}^{-3}], \quad (72)$$

$$T_e = 1.5 \times 10^{11} (r/r_g)^{-8.4}\ [\mathrm{K}], \quad (73)$$

$$B^2/8\pi = 0.1 n_{e,th} m_p c^2 r_g/6r\ [\mathrm{erg\ \ cm}^{-3}]. \quad (74)$$

Here, m_p is the proton mass. The scale height of the accretion flow H is set to be $H/R = 0.5$, where R is the cylindrical radius $R = r \sin\theta$. Only the toroidal component of the magnetic fields is assumed. The cgs-Gauss unit is assumed. The accretion flows are assumed to surround the BH from just outside of the event horizon (i.e., $2r_g$) to $20r_g$ for convenience.

For the SED convergence check, we test the emission and absorption processes of the synchrotron via thermal electrons, synchrotron via nonthermal electrons with a broken power-law distribution, and bremsstrahlung via thermal electrons. The emission coefficients are described by Equations (B5), (B18), and (B19). The broken power-law indices of the nonthermal electrons are $p_1 = 2.5$ and $p_2 = 3.5$ in the range of a Lorentz factor of $\gamma_{e,min} \leqslant \gamma_e \leqslant \gamma_{e.\,br}$ and $\gamma_{e,br} < \gamma_e \leqslant \gamma_{e,max}$, respectively. Here, $\gamma_{e,min} = 30$, $\gamma_{e,max} = 10^6$, and $\gamma_{e,br} = 10^4$. The observers screen is set at $r = 10^4 r_g$ with a field of view (FoV) of $30r_g \times 30r_g$ devided by 300×300 pixels for the calculations with the observer-to-emitter RT algorithm. For the SED computations of the emitter-to-observer MC algorithm, the number of the photon-frequency bins is set to be 50, where the frequency bins divide the photon-frequency space $10^{10}\ \mathrm{Hz} \leqslant \nu \leqslant 10^{23}\ \mathrm{Hz}$ in such a way that the bins are equally spaced in log-scale, i.e., $\Delta \log \nu = 0.26$ (i.e., $\Delta \ln \nu \approx 0.599$). The number of the viewing-angle bins is 100, which divide the viewing angle space $0^\circ \leqslant \theta_{ob} \leqslant 180^\circ$ in such a way that the solid angle of the observer is equally distributed, i.e., $\Delta \cos\theta_{ob} = 2/100$.

The top panels of Figure 13 show the SEDs computed with the emitter-to-observer MC (filled circles) and the observer-to-emitter RT (solid lines) algorithms, respectively. We show SEDs observed with a viewing angle $i = 18.^\circ 2$ (purple), $89.^\circ 4$ (green), and $135.^\circ 2$ (orange). The total SEDs, which we computed by including all the radiative processes, are shown in the leftmost panels. The second, third, and fourth panels from the left represent the SEDs computed by assuming each of the single radiative processes of synchrotron via thermal electrons, the synchrotron via nonthermal electrons with the broken power-law distribution, and the bremsstrahlung via thermal electrons, respectively. The number of the generated superphotons for the MC method is ~10^8. One may find that the SEDs computed with the different two algorithms agree well.

For the convergence check of the MC method, the bottom panels show the integral fractional errors

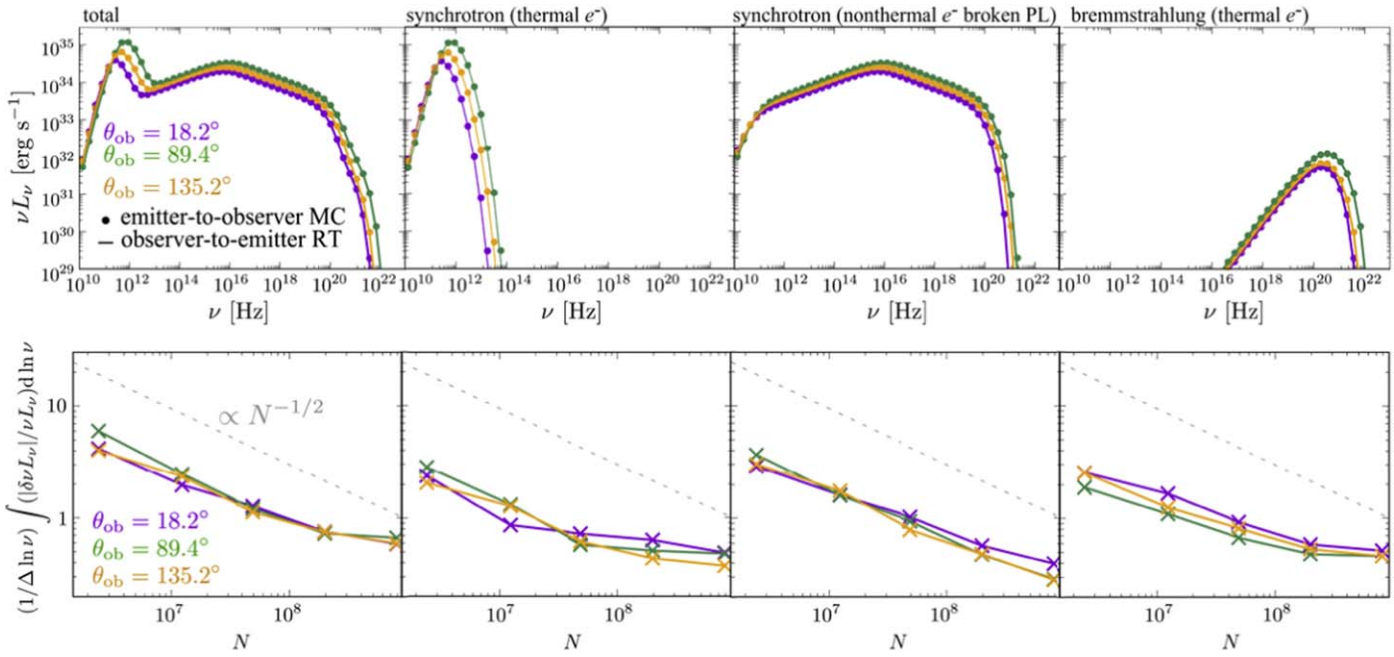

Figure 13. Tests of the radiative transfer calculation with the emitter-to-observer MC algorithm using the Keplerian shell model of radiatively inefficient accretion flows (RIAFs) around a Schwarzschild BH with $M_{BH} = 4.1 \times 10^6 M_\odot$, taking into account the emission and absorption processes of synchrotron via thermal electrons and via nonthermal electrons with a broken power-law distribution ($p_1 = 2.5$ and $p_2 = 3.5$), as well as the bremsstrahlung via thermal electrons. Top: Comparison of the SEDs calculated with the emitter-to-observer MC (filled circles) and observer-to-emitter RT (solid lines) algorithms, respectively. Purple, green, and orange display the results for the viewing angles i=18.°2, 89.°4, and 135.°2, respectively. The width of the photon-frequency bins of the MC calculations is $\Delta \log \nu = 0.26$. Bottom: Integrated fractional errors as a function of the number of the MC-sampled superphotons for each radiative process.

$(1/\Delta \ln \nu) \int [\delta(\nu L_\nu)/\nu L_\nu] d \ln \nu$ for the SEDs of the total and each of the single radiative processes, where $\delta(\nu L_\nu)/\nu L_\nu \equiv (\nu L_{\nu(\mathrm{eo})} - \nu L_{\nu(\mathrm{oe})})/\nu L_{\nu(\mathrm{oe})}$. We define $\nu L_{\nu(\mathrm{eo})}$ and $\nu L_{\nu(\mathrm{oe})}$ as the values computed by the emitter-to-observer MC and the observer-to-emitter RT algorithms, respectively. The results show that the integrated fractional errors are roughly proportional to $N^{-1/2}$, as expected, where N is the total number of the superphotons. We note that the integrated errors decrease relatively slowly with N compared to $N^{-1/2}$. This would be due to the finite value of $\Delta \cos i$, within which the supuperphotons are summed up for each viewing angle in the emitter-to-observer MC algorithm, while the SEDs with the observer-to-emitter RT algorithm are computed for the observer screen with the exact viewing angle. In addition to this, the intensity is computed only at the centers of the pixels in the observer-to-emitter RT algorithm, while the photons are randomly distributed inside each pixel in the emitter-to-observer MC algorithm. This is the reason why the results are not perfectly identical.

Next, we test the convergence of the images computed with the emitter-to-observer MC algorithm. We use the same Keplerian shell model with the calculations of SEDs above, except that we only assume synchrotoron emission and absorption, for simplicity. The setups of the observer screen for the observer-to-emitter RT and the emitter-to-observer MC algorithms are the same as for the SEDs tests. We calculate the images at 230 GHz, where we sum up the superphotons escaping to the observer screen with their photon frequency $220\,\mathrm{GHz} \leqslant \nu \leqslant 240\,\mathrm{GHz}$ for the computations with the emitter-to-observer MC algorithm. The superphtons with the photon frequency $1.53\,\mathrm{GHz} \lesssim \nu \lesssim 1.73\,\mathrm{GHz}$ in the fluid rest frame are generated by taking into account the deviation of the generated photon frequency in the fluid rest frame and the observer frame in the screen, which is caused by the special relativistic Doppler effects and the gravitational redshift.

Figure 14 shows the comparison of the images that we computed with these two methods. The viewing angles are $i = 18.°2$, $89.°4$, and $135.°2$. One may find that the images computed with the emitter-to-observer MC algorithm (center) agree with the image that was computed with observer-to-emitter RT algorithm (left). The error of the resultant radio flux at 230 GHz is within $\sim$0.1%. The right panel shows the distribution of the difference in the computed intensities between these two algorithms at each pixel $\delta I_\nu / I_\nu \equiv (I_{\nu(\mathrm{eo})} - I_{\nu(\mathrm{oe})})/I_{\nu(\mathrm{oe})}$. Here, $I_{\nu(\mathrm{oe})}$ and $I_{\nu(\mathrm{eo})}$ are the specific intensity calculated with the observer-to-emitter RT and the emitter-to-observer MC algorithms, respectively. In the bright region consisting of the photon ring and the innermost accretion disk, the deviation is $\lesssim$10% at each pixel. In the emission from the immediate vicinity of the event horizon, the error becomes $\gtrsim$10%, because the most of generated superhotons are trapped by the BH so that the number of the superphotons is still not enough. The deviation near the polar axis (i.e., $x = 0$ in the screen) is due to the lower accurracy of the Runge–Kutta integration of the geodesic equations, where we reduced the acceptable error for the adoptive stepsize control by more than one order of magnitude to accelerate the computation with the emitter-to-observer MC algorithm. Although the errors in these regions are moderately high, the resultant images do not differ remarkably from each other, because the intensities in these regions are so faint that they hardly affect the signature of the images. It should be noted that the computations of the images with the observer-to-emitter RT algorithm are effectively more than $\sim$700 times faster than the computation with the emitter-to-observer MC algorithm per the viewing-angle bin in this test. It takes $\sim$20 s with 300 cpu cores and $\sim$46.5 hr with 2560 cpu cores with the observer-to-emitter

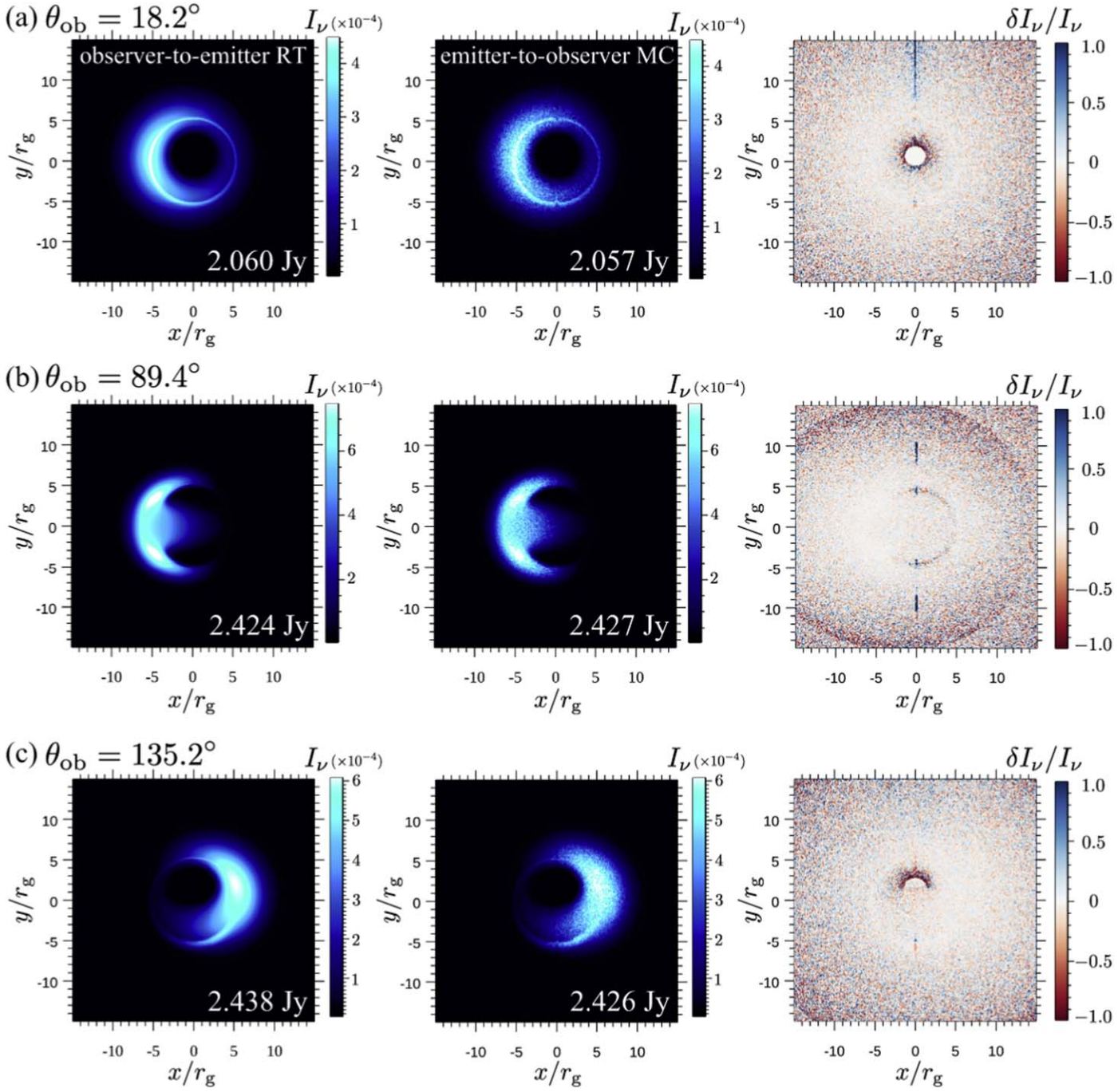

Figure 14. Imaging tests of the MC radiative transfer calculation using the Keplerian shell model of RIAF around a Schwarzschild BH with $M_{\rm BH} = 4.1 M_\odot$. The left and center panels show the images at 230 GHz computed using the observer-to-emitter RT and the emitter-to-observer MC algorithms, respectively. The right panels display the distribution of the relative difference of the computed intensities between these two algorithms at each pixel $\delta I_\nu / I_\nu$. The viewing angles are $i = 18.^\circ 2 =$ (top), $89.^\circ 4$ (middle), and $135.^\circ 2$ (bottom).

RT (1 viewing-angle bin) and emitter-to-observer MC (100 viewing-angle bin for this test) algorithms, respectively. The discrepancy in the computational cost appears to be mainly due to the difference in the number of geodesics to be solved between these two algorithms. We should solve a large number of geodesics of the generated superphotons for the emitter-to-observer MC algorithm.

For the convergence check of the MC method, Figure 15 presents the unweighted spatially averaged relative difference of the resultant images $\langle \delta I_\nu / I_\nu \rangle$ as a function of the number of the MC-sampled superphotons N for the viewing angles $i = 18.^\circ 2$, $89.^\circ 4$, and $135.^\circ 2$. It is confirmed that the averaged relative differences for each viewing angle decrease roughly as $N^{-1/2}$.

7. Application to an Accreting Kerr Black Hole Based on GRMHD Simulations

We show examples of full code tests for which `RAIKOU` was applied to calculate the images and SEDs of the accretion flows, wind, and jets of 3D GRMHD simulation data. For the image computations, we show the radio and X-ray images

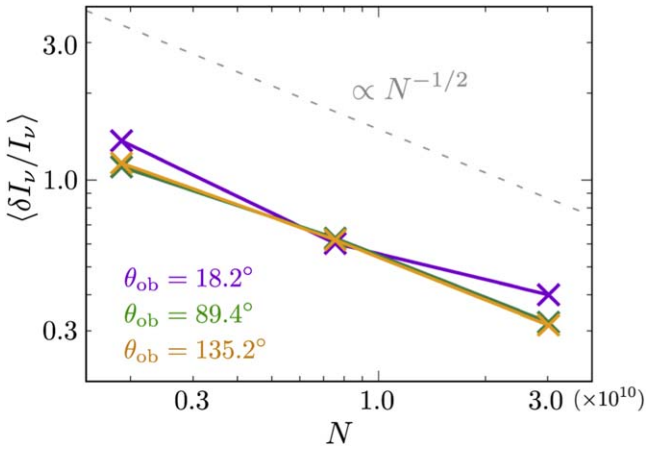

Figure 15. Spatially averaged $\delta I_\nu / I_\nu$ as a function of the number of the MC-sampled superphotons. The viewing angles are $i = 18.^\circ 2$ (purple), $89.^\circ 4$ (green), and $135.^\circ 2$ (orange).

computed by the observer-to-emitter RT and emitter-to-observer MC algorithms, respectively. For the X-ray image calculations, we included the effects of inverse-Compton scatterings. We demonstrate the results of a RIAF around an SMBH where the accretion flows are simulated using the GR-Radiation-MHD code UWABAMI (Takahashi et al. 2016). The key parameters for the GRRT calculations are described below and are summarized in Table 1. The GRMHD simulation data are briefly summarized in Appendix D. For convenience, we use the 3D GRMHD data in the region of $r < 100 r_{\rm g}$ (Figure 16), while the outer boundary of the GRMHD simulation is $3.33 \times 10^3 r_{\rm g}$.

The dimensionless spin parameter a_* is set to be 0.9375. We need to give the scale of the system because GRRT calculations are not scale free. Here, we set the parameters suitable for one of the main targets of EHT, Sgr A*: a BH mass $M_{\rm BH} = 4.1 \times 10^6 M_\odot$, a mass accretion rate $\dot{M} \sim 10^{-8} M_\odot\ {\rm y}^{-1}$, and a distance of the observer screen for the image calculation of $D = 8.1$ kpc.

For the observer-to-emitter RT algorithm, the viewing angle of the observer is set to $\theta_{\rm ob} = 45°$. The FoV of the screen is assumed to be ($10^3\ \mu$as, $10^3\ \mu$as), which is divided by (2.5×10^3, 2.5×10^3) pixels. We also note that the observer screen is set at $\varphi_{\rm ob} = 0°$ in the φ-direction.

To computate multiwavelength SEDs and X-ray images using the emitter-to-observer MC algorithm, we divide the polar angle of the observing photons into 30 bins in such a way that $\Delta \cos\theta_{\rm ob} = 2/30$. As we mentioned in Section 5.5, the $\varphi_{\rm ob}$-averaged images are computed by using the emitter-to-observer MC algorithm, i.e., $\Delta\varphi_{\rm ob} = 2\pi$, to save computational cost in this paper. The FoV for the multiwavelength SED computations is effectively $\sim 10^3\ \mu{\rm as} \times 10^3\ \mu$as because $1 r_{\rm g} \sim 5\ \mu$as for the parameter of Sgr A*, and we restricted the range of GRMHD data witin $100 r_{\rm g}$. The energy bin of the SEDs of the energy band $10^7 {\rm Hz} \leqslant \nu \leqslant 10^{28} {\rm Hz}$ are devided into 55 energy bins, i.e., $\Delta \log \nu \approx 0.382$. To compute X-ray images with the emitter-to-observer MC algorithm, we focus on the FoV of 100 μas $\times$ 100 μas (divided by 160×160 pixels), and photons with energy $1\ {\rm keV} \leqslant h\nu \leqslant 10\ {\rm keV}$ are stacked into one energy bin to briefly demonstrate the images near the BH. The computations of the ray-tracing for the emitter-to-observer MC algorithm continues until the superphotons approach $10^3 r_{\rm g}$ to make images asymptotically the same with those for the observer at infinity, while the GRMHD simulation data are omitted (i.e., radiative processes of emission, absorption, and scattering are omitted) outside $100 r_{\rm g}$ in this work. The total number of the generated superphotons is $N \simeq 7.3 \times 10^{11}$.

Because of the uncertainty of the electron temperature in the GRMHD simulations, we use a formula that describes T_p/T_e as a function of the plasma β, which is so-called R-β prescription (e.g., Mościbrodzka et al. 2016; Event Horizon Telescope Collaboration 2019e),

$$\frac{T_p}{T_e} = \frac{1}{1+\beta^2} R_{\rm high} + \frac{\beta^2}{1+\beta^2} R_{\rm low}, \tag{75}$$

where $R_{\rm high} = 5$ and $R_{\rm low} = 1$. The distribution function of nonthermal electrons is assumed to be a single power law with the power-law index $p = 3.5$. The minimum and maximum Lorentz factors of the nonthermal electrons are $\gamma_{\rm e,min} = 30$ and $\gamma_{\rm e,max} = 10^6$, respectively. The number density of nonthermal electrons is set in such a way that their energy density $u_{\rm e,nth}$ is proportional to that of the magnetic energy density u_B at each computational cell,

$$u_{\rm e,nth} = \eta_{\rm nth} u_B, \tag{76}$$

where the efficiency parameter $\eta_{\rm nth}$ is set to be 0.03 and to be uniform in space in this work.

Figure 17 demonstrates images of accretion flow and jet at 22 (left), 86 (center), and 230 GHz (right), and the broadband SEDs from radio to VHE gamma-ray. The top/middle panels show the images with/without taking into account the effects of nonthermal electrons. The size of the bright region becomes large as a consequence of including the nonthermal electrons, which is consistent with the previous interpretation of Sgr A* using simple toy models (e.g., Özel et al. 2000; Cho et al. 2022). This is because the emissivity via the synchrotron processes is still high in the outer region, while the plasma temperature is low and the thermal synchrotron emission is very faint there. Although the effect of nonthermal electrons is less significant at higher frequency in the radio band, the image taking into account the nonthermal electorns still shows a slightly extended emission image, including compared with that without nonthermal electrons at 230 GHz (i.e., at the photon frequency observing BH shadows by EHT).[8]

The broadband SEDs shown in the bottom panel in Figure 17 present significant differences between the models with and without nonthermal electrons. As is described above, the luminosity in the lower radio band $\lesssim$100 GHz is increased via the nonthermal synchrotron emission. Importantly, the significant number of X-ray photons is generated by the synchrotron emission via nonthermal electrons in addition to the inverse-Compton scattering via the thermal electrons. The SED with thermal and nonthermal electrons (solid red line) at $\sim 10^{17-20}$ Hz is the superposition of the nonthermal synchrotron (dashed red line) plus the SSC via thermal electrons (solid black line). In the gamma-ray band $\gtrsim 10^{20}$, the significant number of photons up to $\sim$TeV is generated by inverse-Compton scattering due to the nonthermal electrons (solid red line), while a low number of gamma-ray photons with $\nu > 10^{22}$

[8] We simply assumed that the energy density of the nonthermal electrons is proportional to the magnetic field energy. If we change the number of the nonthermal electrons based on the local Maxwell–Jüttner distribution, the morphology of the resulting image may change (Davelaar et al., private communication).

Table 1
Set of Parameters for the GRRT Calculation Postprocessing of the GRMHD Simulation

a_*	$M_{\rm BH}(M_\odot)$	D (kpc)	$\dot{M}$ $(M_\odot {\rm y}^{-1})$	$R_{\rm high}$	$R_{\rm low}$	p	$\gamma_{\rm e,min}$	$\gamma_{\rm e,max}$	$\eta_{\rm nth}$	$\theta_{\rm ob}$[a]	FoV[b](μas × μas)
0.9375	4.1×10^6	8.3	$\sim 1 \times 10^{-8}$	13	1	3.5	30	10^6	0.03	45°	$10^3 \times 10^3$

Notes. The set of parameters for the GRMHD simulations is summarized in Appendix D.
[a] The parameter for the observer-to-emitter RT algorithm. For the emitter-to-observer MC algorithm, the results with different viewing angles can be obtained simultaneously.
[b] The parameter for the observer-to-emitter RT algorithm. For the SED computations using the emitter-to-observer MC algorithm, the FoV is effectively 10^3 μas × $10^3$$\mu$as because we restrict the computational domain of the GRRT within $r \leqslant 100 r_{\rm g}$ ($1 r_{\rm g} \sim 5$ μas). For the image computations using the emitter-to-observer MC algorithm, we set the FoV to be 10^2 μas × 10 μas for convenience.

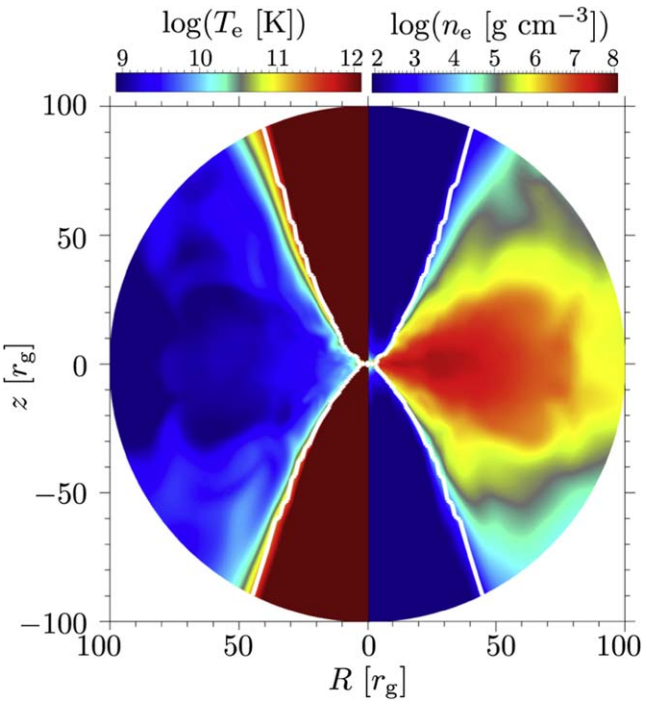

Figure 16. Snapshot of the 3D GRMHD simulation carried out by UWABAMI at $t = 1.2 \times 10^4 r_{\rm g}/c$. The spatial distributions of the electron density $n_{\rm e}$ [g cm^{-3}] (right) and the electron temperature $T_{\rm e}$ [K] (right) at the azimuthal angle $\phi = 0$ are displayed. The cross-section view onto the poloidal plane is presented, where $R = r \sin\theta$ is the cylindrical radius. The electron density is given by setting the mass accretion rate, and electron temperature $T_{\rm e}$ is calculated by adopting Equation (75). The white contour displays the surface of the magnetization $\sigma = 1$, where σ is low in the accretion flow region. We adopt the region with $\sigma \leqslant 1$ for the computations of radiative processes (i.e., emission, absorption, and scattering). The region $r \leqslant 100 r_{\rm g}$, which is used for the radiative transfer in this work, is shown here, while the outer boundary is located at $r = 3.33 \times 10^3 r_{\rm g}$. The detailed structure near the BH is shown in Appendix D.

is emitted in the model with thermal electrons only (solid black line). The power-law shaped SED with the spectral index $\sim(3-p)/2 = -0.25$ expected for synchrotron emmission and inverse-Compton scattering via nonthermal electron appears in the photon-frequency range $10^{16} \lesssim \nu \lesssim 10^{22}$ Hz and $10^{23} \lesssim \nu \lesssim 10^{25}$ Hz, respectively, while the SED shows a slightly complicated structure because of the contribution of the thermal electron processes.

In RIAFs, the effects of the bremsstrahlung emissions from the outer parts of the accretion flows can also be important. The comparison of the thermal SEDs with and without bremsstrahlung is shown in Figure 18. The thermal bremsstrahlung emission can dominate the thermal X-ray emission, as shown in some previsous numerical works (e.g., Yarza et al. 2020; Event Horizon Telescope Collaboration et al. 2022). Although the effects of the inverse-Compton scattering of the photons emitted by bremsstrahlung are incorprated, this is negligible because the bremsstrahlung photons are generated in the outer part of the accretion flows. Figure 19 demonstrates the decomposition of the SEDs with the bremsstrahlung processes into the components of SEDs whose seed photons are emitted in the region near the BH ($r < 10 r_{\rm g}$) or relatively far from the BH ($r \geqslant 10 r_{\rm g}$). One may find that the bremsstrahlung photon emission is dominated by the emission from $r \geqslant 10 r_{\rm g}$. The dominance of the bremsstrahlung emission from the outer part of the accretion flow is consistent with theoretical implications (e.g., Quataert 2002; Yuan et al. 2003), while the caveat is that the remaining remnant of the initial accreting torus may enhance the bremsstrahlung for the simulations with the initial torus setup.

In Figure 20, the SEDs are decomposed into the components of nonscattered photons, photons scattered once, and photons scattered twice. The SEDs of synchrotron and Compton processes via thermal and nonthermal electrons, the SED via thermal electrons alone, and the synchrotron, bremsstrahlung, and Compton processes via thermal electrons alone are presented. The viewing angle of the observer is 45°.6. The features of nonscattered and scattered components appear reasonably clearly. Here, we note that the SEDs of the synchrotron and Compton processes via thermal and nonthermal electrons show that the one-scattering photons show harder SEDs than two-scattering photons. This is caused by the significant decrease in the Klein–Nishina cross section of the high photon energy, which is measured in the rest frame of scattering electrons with nonthermal distribution, which is greater than the electron rest-mass energy.

Figure 21 shows the dependence of the SEDs on the viewing angles. Beacause of the relativistic Doppler effects due to the rotation of the accretion flows in the vicinity of the BH, the emission in $10^{11} \lesssim \nu \lesssim 10^{14}$ Hz is brighter for higher inclination cases. For the same reason, the bumps formed by the inverse-Compton scattering at 10^{16} Hz $\lesssim \nu \lesssim 10^{22}$ Hz shows a higher luminosity for the case of the higher viewing angle because the effects of Compton upscattering of synchrotron photons are most remarkable in the region near the BH. These are consistent with the similar computation of Mościbrodzka et al. (2009). We note that the synchrotron emission in $\nu \sim 10^{15}$ Hz and its Comptonized emission in $\nu \gtrsim 10^{22}$ Hz is bright for the low viewing angle $\theta_{\rm ob} = 14.8$ due to the relativistic Doppler effects by the bulk motion of jet funnel (i.e., the transition layer between the relativistic jets and the accretion flows/winds). For the SSC with the bremsstrahlung model, we note that the bremsstrahlung emission, which appears at 10^{18}Hz $\lesssim \nu \lesssim 10^{21}$ Hz, is almost isotropic. This is because the breamsstrahlung

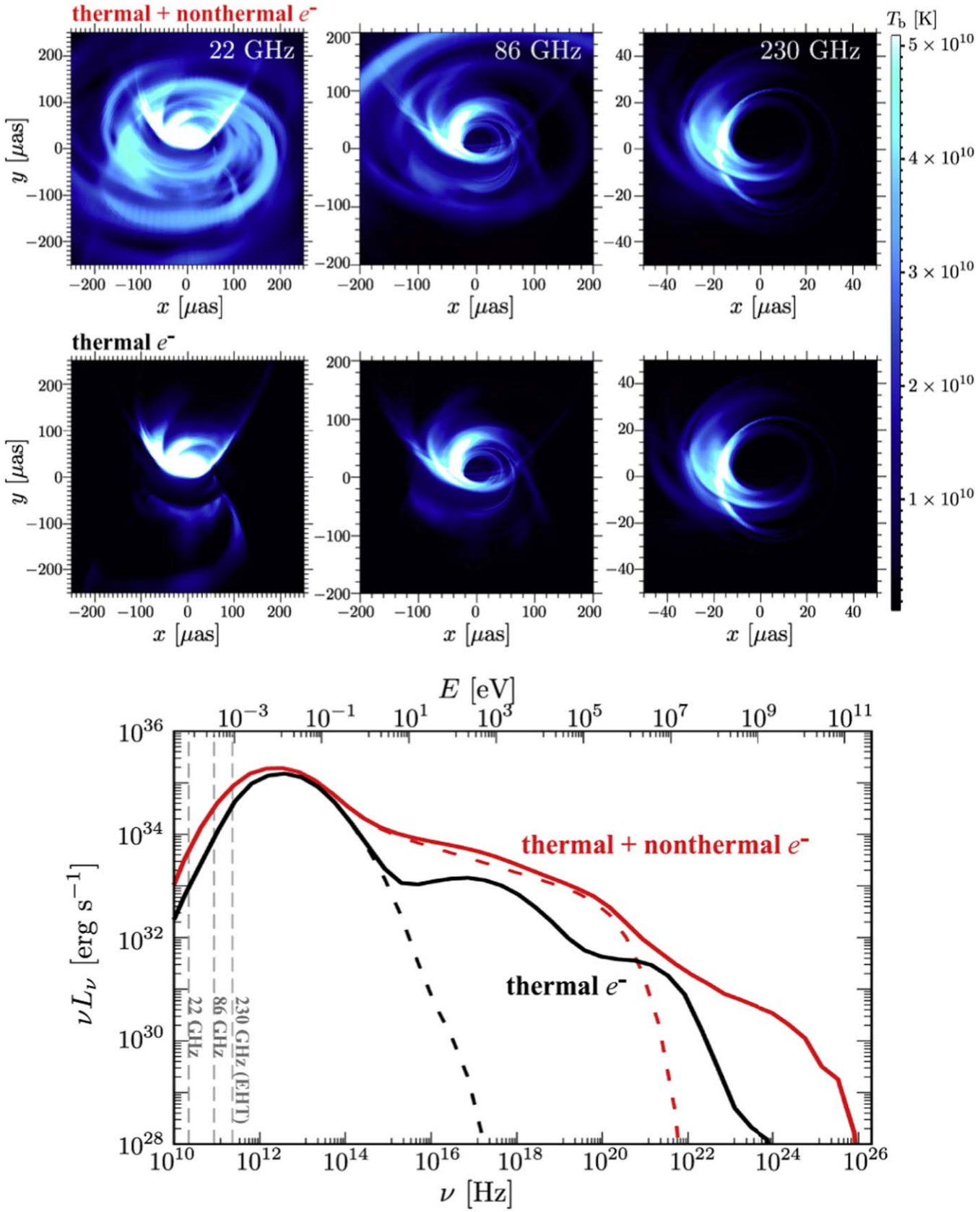

Figure 17. Top: multifrequency radio images of the GRMHD simulation model of RIAF, which are computed with the observer-to-emitter RT algorithm, taking into account the synchrotron emission and absorption via thermal and nonthermal electrons. The image is shown in units of brightness temperature. Middle: the same as in the top panels, but only the thermal electrons are taken into account. Bottom: the SEDs calculated with the emitter-to-observer MC algorithm, taking into account the thermal and nonthermal electorns (red) and thermal electrons only (black). The synchrotron emission/absorption and inverse-Compton/Compton scattering processes are incorporated. The solid and dashed lines show the SED with and without the inverse-Compton scattering, respectively. The width of the photon-frequency bin is $\Delta \log \nu \approx 0.382$. The viewing angle is $\theta_{\rm ob} = 45.^\circ 6 \approx 45^\circ$. The vertical dashed gray lines represent the photon frequencies at 22, 86, and 230 GHz.

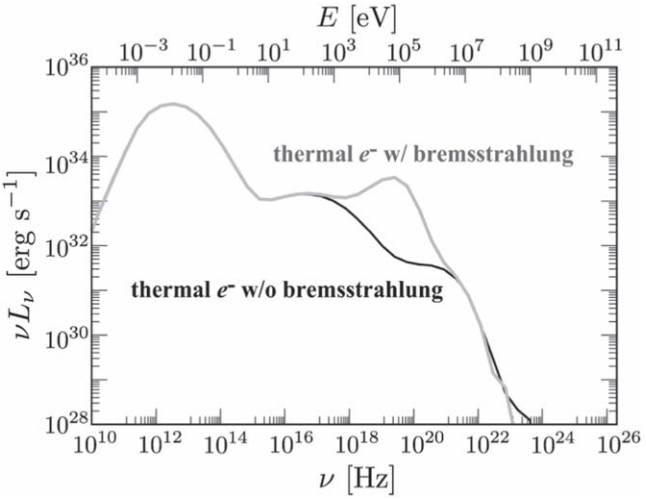

Figure 18. The SED of the GRMHD simulation model of RIAF with and without thermal bremsstrahlung emission and absorption (gray line). As a reference, the SED without bremsstrahlung processes, which is the same as the SED of the thermal electron model shown in Figure 17, is shown as the solid black line. To compute the two SEDs, the synchrotron emission/absorption and Compton/inverse-Compton scattering via thermal electrons are included.

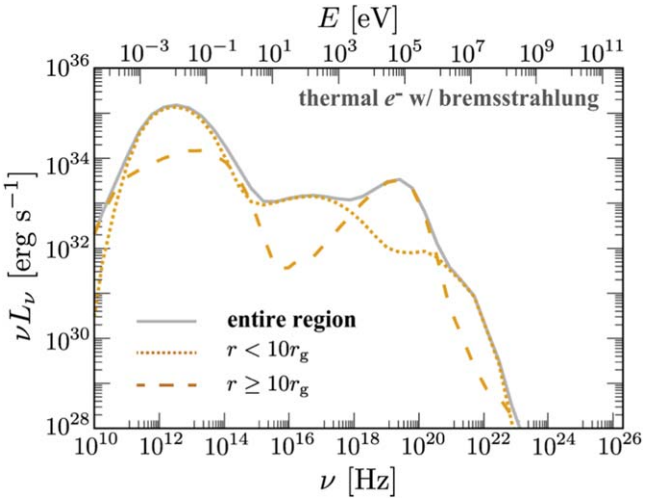

Figure 19. Decomposition of SEDs with thermal bremsstrahlung emission/absorption (solid gray line) into the components whose seed photons are emitted in the region $r < 10r_g$ (dotted orange line) and $r \geqslant 10r_g$ (dashed orange lines), the emission regions.

emission occurs in the outer disk region, where the bulk motion is subrelativistic and the plasma is optically thin against the bremsstrahlung process. It should be noted that the statistical noise still appears in the gamma-ray energy range $10^{22}\,\mathrm{Hz} \lesssim \nu \lesssim 10^{24}\,\mathrm{Hz}$ for a low viwing angle of $\theta_{\rm ob} = 14.^{\circ}8$.

Next, we demonstrate the computations of X-ray shadow images. Because the inverse-Compton scatterings are important for the computations of X-ray images, we solve the GRRT with the emitter-to-observer MC algorithm. Figure 22 displays the images of the escaped photons of $1\,\mathrm{keV} \leqslant h\nu \leqslant 10\,\mathrm{keV}$ emitted by the synchrotron and Compton processes via thermal plus nonthermal electrons, those via thermal electrons alone, and the synchrotron, Compton, and bremsstrahlung processes with thermal electrons alone. The results with the viewing angle $\theta_{\rm obs} = 45.^{\circ}6$ are shown. The left, center, and right panels display the images of total photons (i.e., photons including the scattered and unscattered ones via inverse-Compton process),

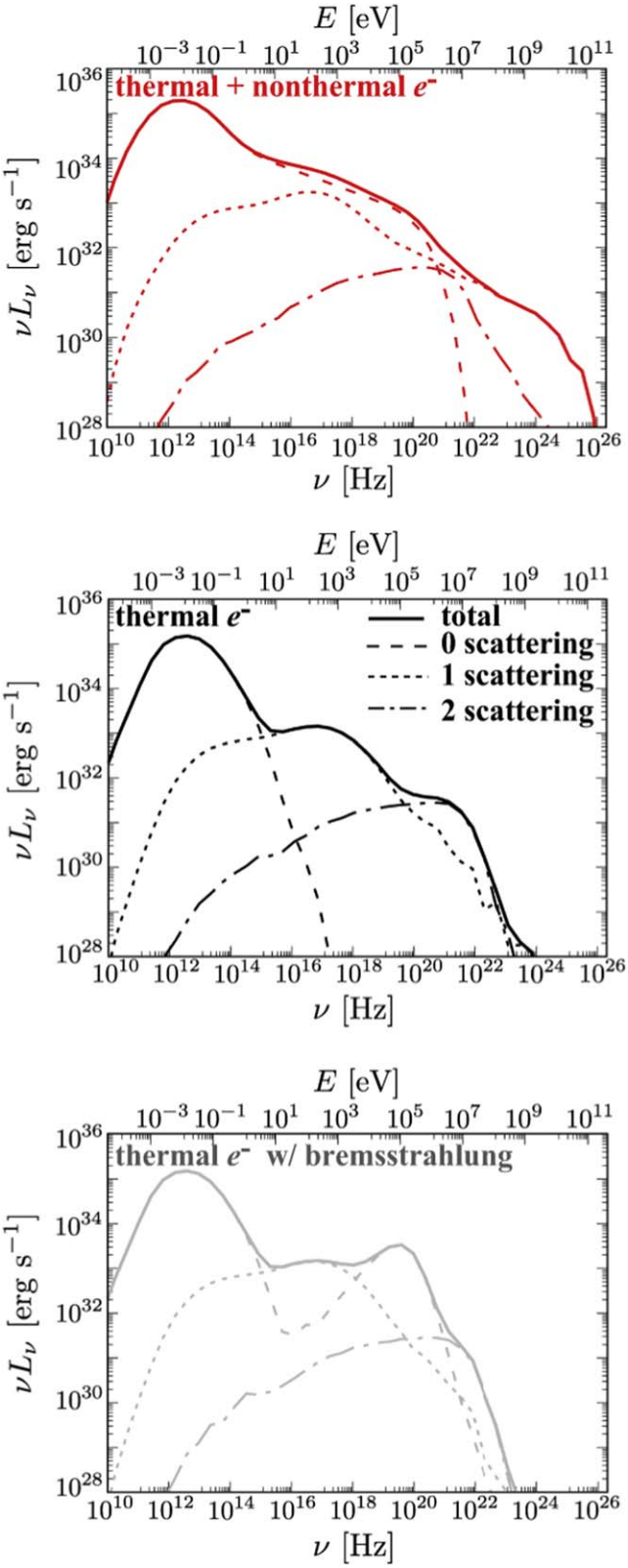

Figure 20. The decomposition of the SEDs into the components of nonscattered photons (dashed lines), photons scattereced once (dotted lines), and photons scattered twice (dot–dashed lines). The total SED is described by the solid lines. The SEDs of synchrotron and Compton processes via thermal and nonthermal electrons (top), the SED via thermal electrons alone (middle), and synchrotron, bremsstrahlung, and Compton processes via thermal electrons alone (bottom) are displayed. The viewing angle is $45.^{\circ}6$. The SEDs are computed with the emitter-to-observer MC algorithm.

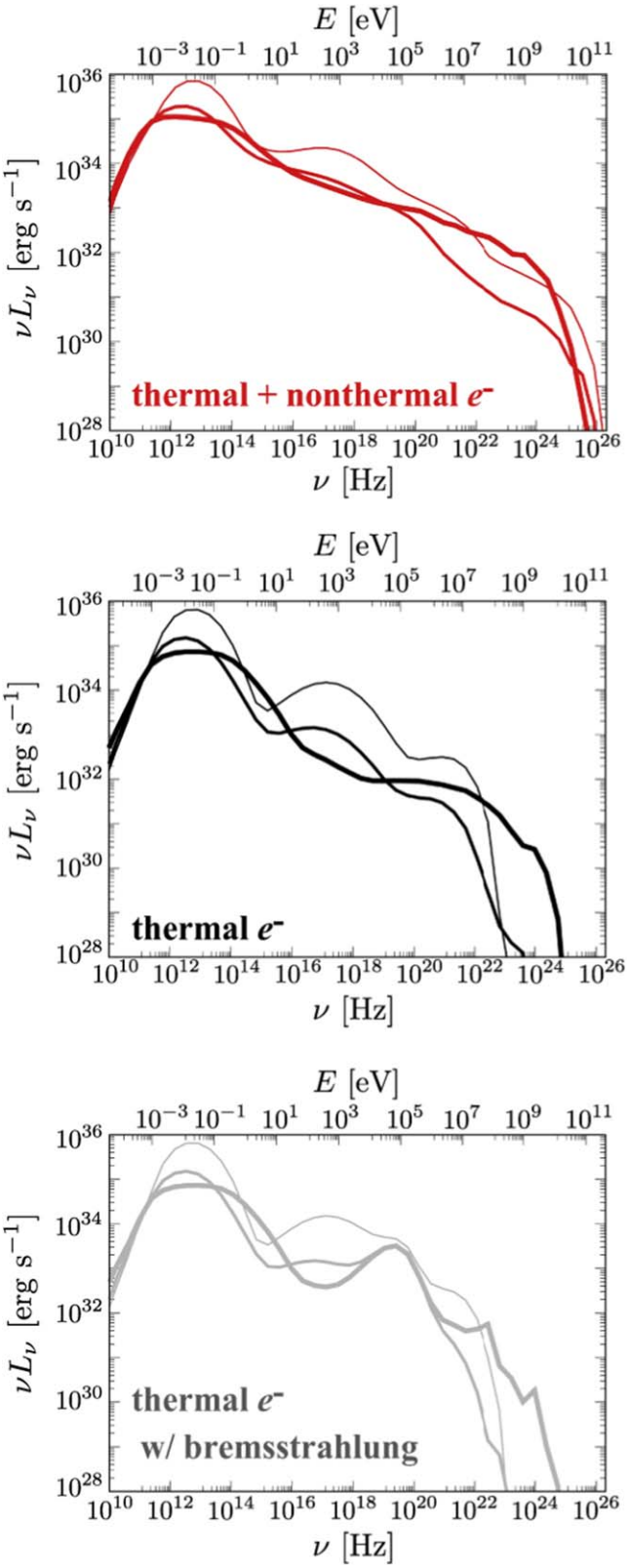

Figure 21. The dependence of SEDs on the viewing angle for the models of SSC via thermal plus nonthermal electrons (top panel), SSC via thermal electrons (middle panel), and SSC with bremsstrahlung via thermal electrons (bottom panel). The SEDs for the viewing angles 14.°8, 45.°6, and 88.°1 are presented as thick, moderate, and thin lines, respectively.

nonscattered photons, and scattered photons, respectively. One may find that the images of the models with thermal electrons alone (i.e., middle and bottom rows) are dominated by the scattered photons and form the crescent-like photon-ring images. The scattered photons can still form the photon ring, because the SSC processes are dominant in the vicinity of the BH and the scattered photons can propagate around the photon sphere.

The dominance of the Compton-upscattered components for the model of the synchrotron and Compton processes via the thermal electrons is consistent with the SED shown in Figure 17. The model of the synchrotron, Compton, and bremsstrahlung processes via the thermal electrons shows the same images as those without bremsstrahlung because the bremsstrahlung emission is dominated by the emission outside $10r_{\rm g}$, i.e., $\sim$50 μas for Sgr A*, as shown in Figure 19. The nonthermal synchrotron emission can enhance the emission of and around the photon ring, because the nonscattered nonthermal synhcrotron emissions and Compton-upscattered photons can both contribute the emission for the nonthermal model, as shown in Figure 17.

In order to show the dependence of the X-ray shadow images on the radiative processes and the nonthermal electrons more clearly, Figure 23 displays the log-scale intensity images with varying viewing angle $\theta_{\rm ob}$. One may find that the nonthermal synchrotron emissions enhance the emission around the photon ring. On the other hand, incorporating the bremsstrahlung emissions does not change the images near the BH, except for the fairly faint additional disk emission with the moderately relativistic Doppler effect appearing on the observer screen $y \sim 0$ μas and $x < 0$ μas for $\theta_{\rm ob} = 88.^\circ1$. This indicates that the future observation by the X-ray interferometer, which is planned to approach a resolution of $\sim$1 μas for the optimistic case (Hayashida et al. 2020; Uttley et al. 2021), may enable us to detect the X-ray BH shadow images and constrain the physics of nonthermal electron accelerations in the vicinity of BHs by subtracting the possible contamination of the X-ray emission of the bremsstrahlung emission in the outer part of the accretion flows.

We check the consistency between the two algorithms, i.e., the observer-to-emitter RT and the emitter-to-observer MC algorithms. Figure 24 shows the SEDs calculated with the observer-to-emitter RT and emitter-to-observer MC algorithms, where the Compton effects are not included for the comparison because the observer-to-emitter RT algorithm cannot solve the Compton scattering. The SEDs with the former algorithms are averaged in the azimuthal direction to compare with the latter ones because our broadband SEDs are computed by summing up over the azimuthal angle φ and averaged as in `grmonty` (Dolence et al. 2009). One may find that the SEDs computed by the different methods are mutually consistent, except for a small difference in $\nu \sim 10^{15-16}$ Hz, i.e., the SEDs slightly deviate due to the relativistic Doppler effects caused by the relativistic bulk motion in the jet between $10r_{\rm g} \leqslant r < 30r_{\rm g}$. It should be also noted that the deviation is still $\lesssim$(several) times 10% at the highest peak in the entire frequency range of the SEDs, which will be enough to compare the theoretical SEDs with observation data. The radio emission, which is crucial for the comparison with the EHT data, is nearly identical between the two different calculation algorithms.

The results of the self-convergence test for our broadband SED calculations are shown in Figure 25. We used the SEDs with $N \simeq 7.3 \times 10^{11}$ shown in Figure 17 for reference, where N is the total number of superphotons. As expected, the relative errors accumulated over the photon-frequency bins decrease

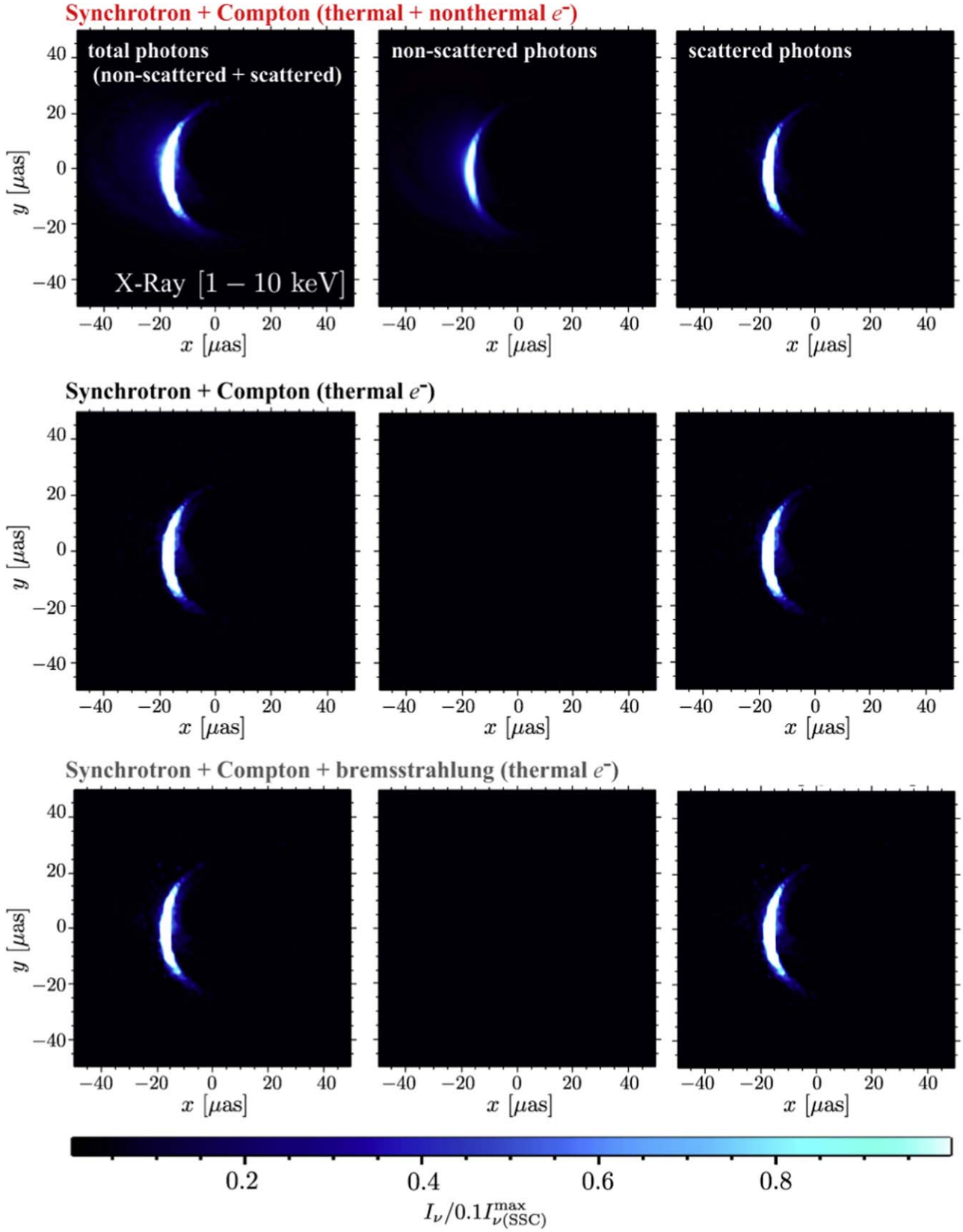

Figure 22. Linear-scale X-ray shadow images (1 keV $\leqslant h\nu \leqslant$ 10 keV) of the GRMHD-RIAF model as in Figure 17. The viewing angle is $\theta_{\rm ob} = 45.^{\circ}6$. The images are averaged in the $\varphi_{\rm ob}$-direction. Top panels: synchrotron emission/absorption and Compton/inverse-Compton scattering via thermal plus nonthermal electrons. Middle panels: synchrotron emission/absorption and Compton/inverse-Compton scattering via thermal electrons alone. Bottom panels: synchrotron emission/absorption, bremsstrahlung emission/absorption, and Compton/inverse-Compton scattering via thermal electrons alone. Total, nonscattered, and scattered photon images are shown in the left, center, and right columns, respectively. The intensities in all panels are normalized by 10% of the maximum value for the model with synchrotron emission/absorption and Compton/inverse-Compton scattering via thermal electrons alone (i.e., the middle left panel).

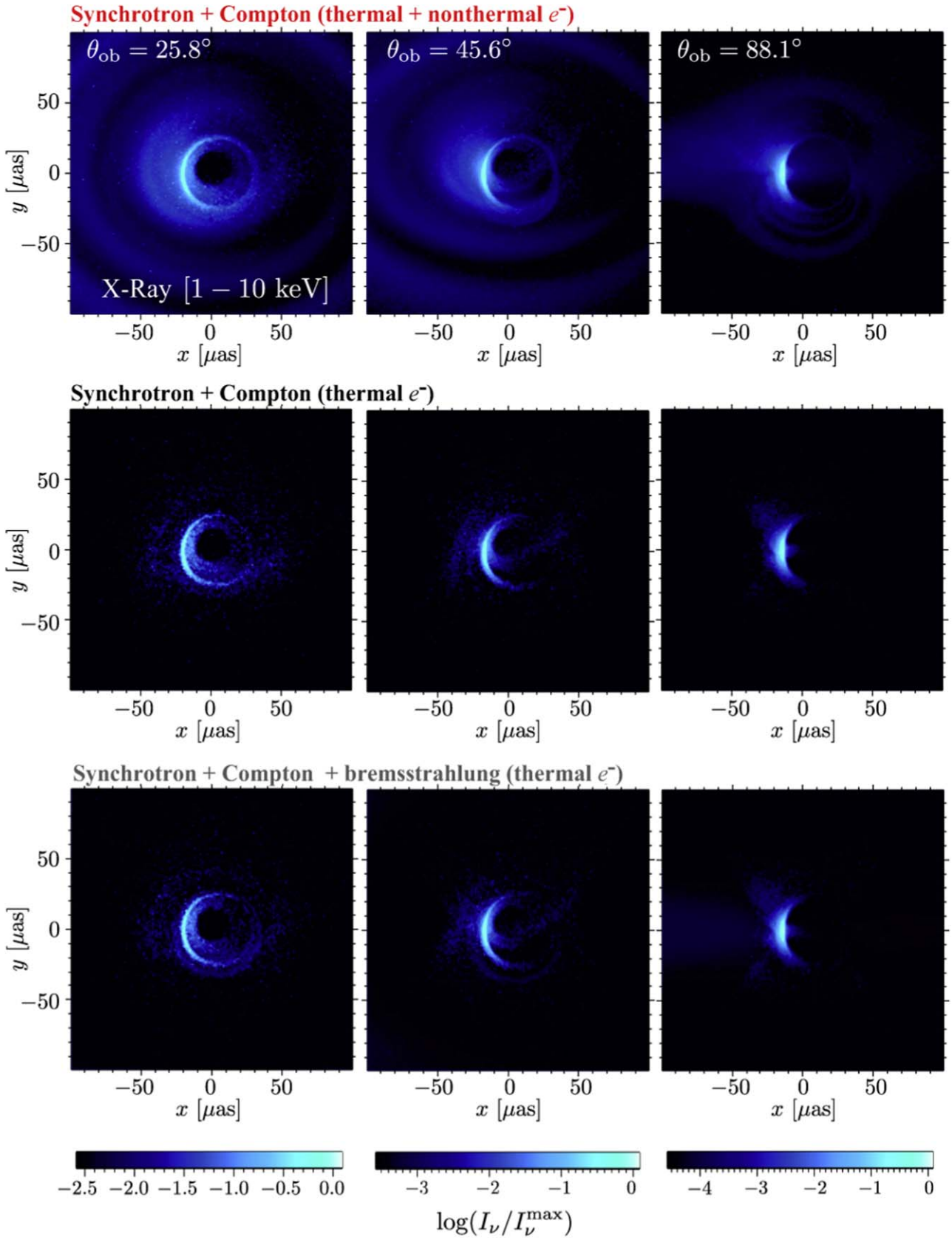

Figure 23. Log-scale X-ray shadow images (1 keV $\leqslant h\nu \leqslant$ 10 keV) of the same GRMHD-RIAF model as in Figures 17 and 22. The viewing angle is $\theta_{ob} = 25.^\circ8$ (left), $45.^\circ6$ (center), and $88.^\circ1$ (right). The images are averaged in the φ_{ob}-direction. Synchrotron and Compton processes via thermal plus nonthermal electrons (top), those via the thermal electron alone (middle), and synchrotron, Compton, and bremsstrahlung processes via thermal electron alone (bottom) are considered.

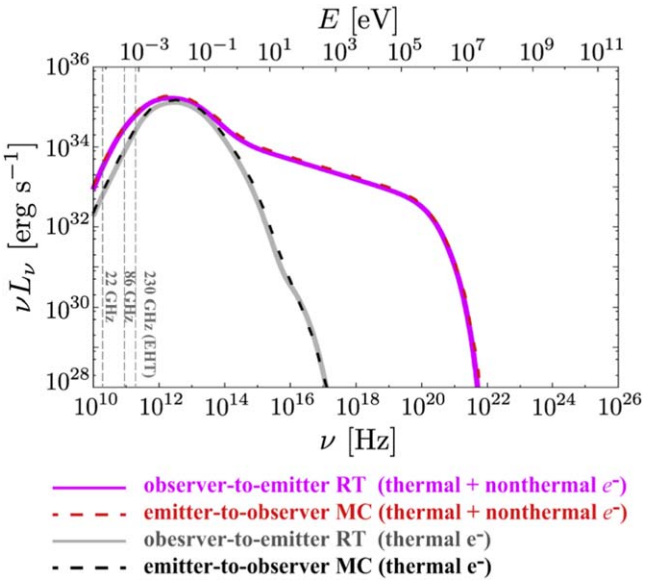

Figure 24. Comparison of SEDs calculated with the observer-to-emitter RT (solid lines) and the emitter-to-observer MC algorithm (dashed lines). The results with thermal plus nonthermal electrons are shown in magenta and red, while those with thermal electrons alone are shown in gray and black.

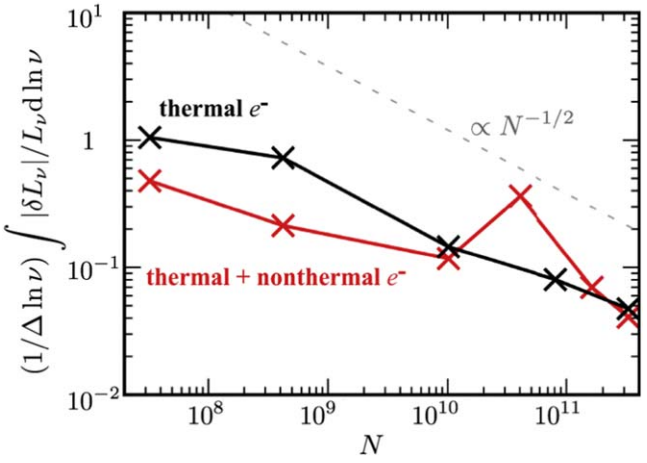

Figure 25. Integrated fractional error as a function of the number of generated superphotons for the model with thermal and nonthermal electrons (red) and thermal electrons alone (black), respectively. The dashed gray line indicates the error proportional to $N^{-1/2}$ as reference.

roughly as $N^{-1/2}$ for the models with and without the nonthermal electrons.

To compute multiwavelength SEDs with the emitter-to-observer MC algorithm, which are shown in Figure 17, it takes ∼13,728 node hours for the emission model of the synchrotron and Compton processes via thermal and nonthermal electrons, and ∼4,541 node hours for those via thermal electrons alone. The computations are carried out on a Cray XC50 system, where two Intel Xeon Skylakes 6148 (20 cores, 2.4 GHz, 1.536 TFlops) are implemented per node. The current high computational cost is mainly due to the eigth-order Runge–Kutta algorithm for the geodesic solver. The acceleration of the calculation through the code optimization remains for future work.

8. Summary and Discussion

We have developed the multiwavelength general relativistic radiative transfer code RAIKOU (来光) to compute the multiwavelength images and SEDs of accreting Kerr BHs in the broadband energy bands from radio to VHE gamma-rays, based on a ray-tracing method. The two different algorithms are implemented in RAIKOU, which is an observer-to-emitter RT algorithm for efficient calculations of images and an emitter-to-observer MC algorithm for computations of broadband SEDs by incorporating the inverse-Compton scattering of soft photons via themal and nonthermal electrons.

The radiative processes of cyclo-synchrotron emission/absorption via thermal electrons, synchrotron emission/absorption via thermal and nonthermal electrons, bremsstrahlung emission/absorption via thermal electrons, and inverse-Compton/Compton scattering via thermal and nonthermal electrons are incorporated. The implementation of these important radiative processes into the code enabled us to calculate detailed images and broadband SEDs, with the broad energy band ranging from radio to VHE gamma-rays. The nonthermal synchrotron emission will enlarge the bright region in the resulting images, and X-ray and gamma-ray emissions are significantly increased due to the combination of the nonthermal synchrotron emission and the inverse-Compton scattering via the nonthermal electrons, respectively. These will be useful to constrain the physical parameters in the main target of EHT, i.e., Sgr A* and M87, and other accreting BHs. Although we focused on the application to the calculations for RIAFs in this paper, our code can be applied to studies of the super-Eddington accretion flow around BHs and neutron stars, which will be realized in ultraluminous X-ray sources and tidal disruption events. We leave this for future work.

We have also demonstrated the capability of the calculation of the X-ray BH shadow images that are formed by the synchrotron emission due to nonthermal electrons and SSC photons. It is shown that the Compton scattering processes can form the photon ring and that the nonthermal synchrotron emission enhances the brightness of and around the X-ray photon ring. The contribution of the bremsstrahlung emission from the outer accretion flow, which can dominate the X-ray SED, can be subtracted when we observe the horizon-scale X-ray images through the future X-ray interferometry missions (Hayashida et al. 2020; Uttley et al. 2021). It may enable us to focus on the discussion of synchrotron and inverse-Compton processes near the BHs, and to constrain the acceleration mechanism of the nonthermal electrons in the vicinity of the BHs. Further studies of the nonthermal-electron modeling are left for future work.

In the current version of our code, the $e^{\pm}$ creation and annihilation via the γ-γ collision, which will be important for studying the formation of the $e^{\pm}$ jet (Wong et al. 2021) and the SEDs in VHE gamma-ray bands absorbed by the intrinsic photons and the extragalactic background light. While the latter effect, i.e., the absorption of VHE gamma-rays via pair creation due to the interaction with extragalactic background light, is negligible for studying the Galactic center and nearby low-luminosity active galactic nuclei, which are the main targets of EHT (e.g., Sgr A* and M87), it is important to incorporate it when we extend our study to the SEDs of distant active galactic nuclei (e.g., MAGIC Collaboration et al.). It should be also mentioned that we focused on the leptonic radiative mechanism. The incorporation of hadronic processes, e.g., *p*-*p* and *p*-

γ collision and successive production of gamma-ray photons via the decay of pions, as well as the production of high-energy neutrinos via the decay of charged pions, will be future works. The direct synchrotron emission via accelerated protons will also contribute to the VHE gamma-ray emission. The effects of the bremsstrahlung emission via nonthermal electrons should be incorporated in future work. In our demonstration, the fast-light approximation (i.e., the snapshot data are fixed during the radiative transfer calculation) is used. For more precise calculations and the study of the time-variable images and SEDs, it will be important to use the snapshot depending on the physical time during the GRRT computation. The inclusion of these effects will be addressed in the near future.

We thank M. Kino, I. Cho, K. Kawaguchi, and K. Asano for fruitful discussion, and the anonymous referee for helpful comments that significantly improved this paper. The numerical simulations were carried out on the XC50 at the Center for Computational Astrophysics, National Astronomical Observatory of Japan. This work also used the computational resources of the supercomputer Fugaku provided by RIKEN through the HPCI System Research Project (Project ID: hp120286). This work was supported by JSPS KAKENHI grants Nos. JP18K13594, JP19H01908, JP19H01906 (T.K.), JP18K03710, JP21H04488 (K.O.), JP20K11851, JP20H01941, JP20H00156 (H.R.T). This work was also supported in part by MEXT SPIRE, MEXT as "Priority Issue on post-K computer" (Elucidation of the Fundamental Laws and Evolution of the Universe) and as "Program for Promoting Researches on the Supercomputer Fugaku" (Toward a unified view of the universe: from large scale structures to planets), and JICFuS.

Appendix A
Electron Distribution Function

A.1. Formalism

A.1.1. Maxwell–Jüttner Distribution

The distribution function of relativistic thermal electrons, i.e., the Maxwell–Jüttner distribution, is described as

$$\frac{dn_{\rm e,th}}{d\gamma_{\rm e}} = \frac{n_{\rm e,th}}{\Theta_{\rm e}} \frac{\gamma_{\rm e}^2\sqrt{1-\gamma_{\rm e}^{-2}}}{K_2(\Theta_{\rm e}^{-1})} \exp\left(-\frac{\gamma_{\rm e}}{\Theta_{\rm e}}\right), \tag{A1}$$

where $n_{\rm e,th}$ is the number density of thermal electrons, $\gamma_{\rm e}$ is the Lorentz factor of the thermal electron motions, K_2 is the modified Bessel function of the second kind, $\Theta_{\rm e} = k_{\rm B}T_{\rm e}/m_{\rm e}c^2$ is the dimensionless electron temperature, $T_{\rm e}$ is the electron temperature, $k_{\rm B}$ is the Boltzmann constant, $m_{\rm e}$ is the electron mass, and c is the speed of light.

A.1.2. Single Power-law Distribution

The single power-law distribution $dn_{\rm e,nth}/d\gamma_{\rm e} \propto \gamma_e^{-p}$ between $\gamma_{\rm e,min} \leqslant \gamma_{\rm e} \leqslant \gamma_{\rm e,max}$ is written as

$$\frac{dn_{\rm e,nth}}{d\gamma_{\rm e}} = \frac{n_{\rm e,nth}(1-p)}{\gamma_{\rm e,max}^{1-p} - \gamma_{\rm e,min}^{1-p}} \gamma_{\rm e}^{-p} \ (\text{for } p \neq 1), \tag{A2}$$

$$\frac{dn_{\rm e,nth}}{d\gamma_{\rm e}} = \left[\ln\left(\frac{\gamma_{\rm e,max}}{\gamma_{\rm e,min}}\right)\right]^{-1} \gamma_{\rm e}^{-p} \ (\text{for } p = 1). \tag{A3}$$

A.1.3. Broken Power-law Distribution

Alternatively, one can use the broken power-law distribution function, in which electrons with different power-law indices are distributed as $dn_{\rm e,nth}/d\gamma_{\rm e} \propto \gamma_{\rm e}^{-p_1}$ between the range $\gamma_{\rm e,min} \leqslant \gamma_{\rm e} \leqslant \gamma_{\rm e,br}$ and $dn_{\rm e,nth}/d\gamma_{\rm e} \propto \gamma_{\rm e}^{-p_2}$ between the range $\gamma_{\rm e,br} < \gamma_{\rm e} \leqslant \gamma_{\rm e,max}$.

For $p_1 \neq 1$ and $p_2 \neq 1$,

$$\frac{dn_{\rm e,nth}}{d\gamma_{\rm e}} = {\rm A} n_{\rm e,nth}\gamma_{\rm e}^{-p_1} \ (\text{for } \gamma_{\rm e,min} \leqslant \gamma_{\rm e} \leqslant \gamma_{\rm e,br}), \tag{A4}$$

$$\frac{dn_{\rm e,nth}}{d\gamma_{\rm e}} = {\rm A} n_{\rm e,nth}\gamma_{\rm e,br}^{-p_1+p_2}\gamma_{\rm e}^{-p_2} \ (\text{for } \gamma_{\rm e,br} < \gamma_{\rm e} \leqslant \gamma_{\rm e,max}), \tag{A5}$$

where

$$A \equiv \left[\frac{\gamma_{\rm e,br}^{1-p_1} - \gamma_{\rm e,min}^{1-p_1}}{1-p_1} + \frac{\gamma_{\rm e,br}^{-p_1+p_2}(\gamma_{\rm e,max}^{1-p_2} - \gamma_{\rm e,br}^{1-p_2})}{1-p_2}\right]^{-1}. \tag{A6}$$

A.2. Methodology of MC Sampling

A.2.1. Maxwell–Jütter Distribution

Using the same procedure as Canfield et al. (1987), we sample the electrons with the Maxwell–Jütter Distribution as follows:

1. We generate a pseudo-random number ξ_1 to select $i(=3, 4, 5, 6)$ of the function π_i in the following equation:

$$\pi_3(\Theta_{\rm e}) = \frac{1}{S_3(\Theta_{\rm e})}\frac{\sqrt{\pi}}{4}, \tag{A7}$$

$$\pi_4(\Theta_{\rm e}) = \frac{1}{S_3(\Theta_{\rm e})}\frac{1}{2\sqrt{2}}\Theta_{\rm e}^{1/2}, \tag{A8}$$

$$\pi_5(\Theta_{\rm e}) = \frac{1}{S_3(\Theta_{\rm e})}, \frac{3\sqrt{\pi}}{8}\Theta_{\rm e} \tag{A9}$$

$$\pi_6(\Theta_{\rm e}) = \frac{1}{S_3(\Theta_{\rm e})}\frac{1}{\sqrt{2}}\Theta_{\rm e}^{3/2}, \tag{A10}$$

   where $S_3(\Theta_{\rm e})$ is described as follows:

$$S_3(\Theta_{\rm e}) = \frac{\sqrt{\pi}}{4} + \frac{1}{2\sqrt{2}}\Theta_{\rm e}^{1/2} + \frac{3\sqrt{\pi}}{8}\Theta_{\rm e} + \frac{1}{\sqrt{2}}\Theta_{\rm e}^{3/2}. \tag{A11}$$

   Obviously, $\sum_{i=3}^{6}\pi_i(\Theta_{\rm e}) = 1$ and i can be determined by using the pseudo-random number $0 \leqslant \xi_1 \leqslant 1$.

2. Using the chosen i, we generate the random number ξ_2 reproducing g_i, which is the χ^2 distribution of order i,

$$g_3(\xi_2) = \frac{4}{\sqrt{\pi}}(\xi_2)^2\exp[-(\xi_2)^2], \tag{A12}$$

$$g_4(\xi_2) = 2(\xi_2)^3\exp[-(\xi_2)^2], \tag{A13}$$

$$g_5(\xi_2) = \frac{8}{3\sqrt{\pi}}(\xi_2(^5\exp[-(\xi_2)^2], \tag{A14}$$

$$g_6(\xi_2) = (\xi_2)^5\exp[-(\xi_2)^2], \tag{A15}$$

   where ξ_2 is distributed as $-\infty < \xi_2 < \infty$.

3. The generated ξ_2 is acceptable if it satisfies

$$\frac{\sqrt{1+(\xi_2)^2\Theta_{\rm e}}}{1+\xi_2\sqrt{\Theta_{\rm e}/2}} \geqslant \xi_3, \tag{A16}$$

   where ξ_3 $(0 \leqslant \xi_3 \leqslant 1)$ is a newly generated random

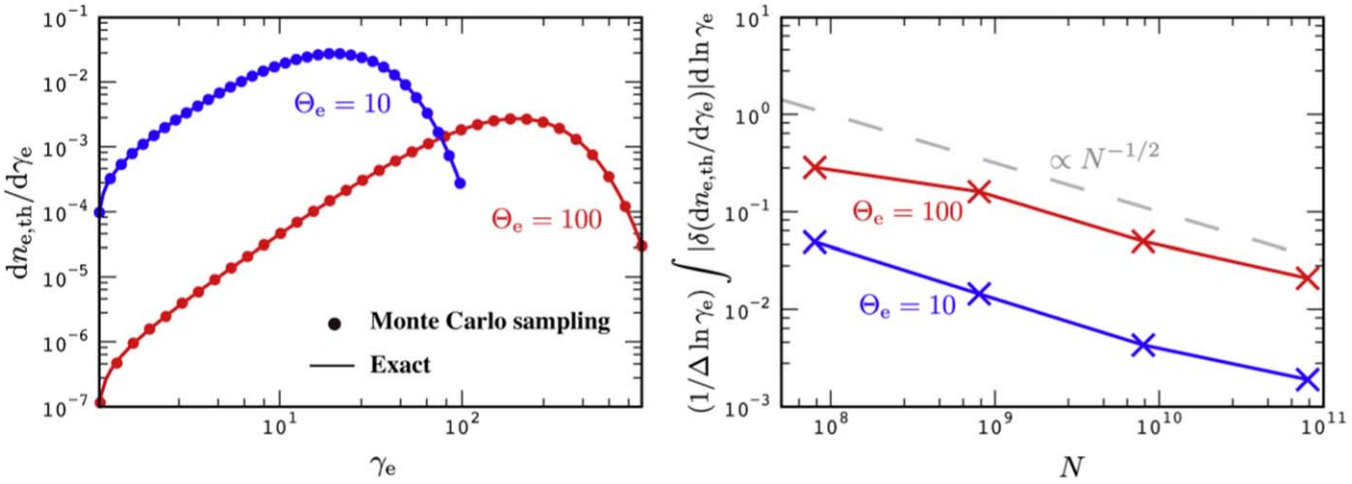

Figure 26. Left: thermal electron distribution functions with the Maxwell–Jüttner distribution. Filled circles and solid lines represent the result obtained by the MC sampling and the exact results described by the equation, respectively. The results of the dimensionless temparatures $\Theta_e = 10$ and 100 are displayed in blue and red, respectively. Right: integrated fractional errors as a function of the number of the MC-sampled electrons.

number for the rejection method. The Lorentz factor of the electron is given by

$$\gamma_e = 1 + (\xi_2)^2. \tag{A17}$$

If the above condition is not satisfied, then we return to step 1. The procedure repeats until the condition is satisfied.

A.2.2. Single Power-law Distribution

On the other hand, for nonthermal electrons with a single/broken power-law distribution, the Lorentz factor of the scattering electrons can be sampled much easier by the inverse function method. For a single power-law distribution, the Lorentz factor can be represented by generating the pseudo-random number ξ,

$$\gamma_e = \gamma_{\min}\left[1 + \xi\left\{\left(\frac{\gamma_{e,\max}}{\gamma_{e,\min}}\right)^{1-p} - 1\right\}\right]^{1/(1-p)} \quad (\text{for } p \neq 1), \tag{A18}$$

$$\gamma_e = \gamma_{\min}\left(\frac{\gamma_{e,\max}}{\gamma_{e,\min}}\right)^{\xi} \quad (\text{for } p = 1). \tag{A19}$$

A.2.3. Broken Power-law Distribution

For a broken power-law distribution, the Lorentz factor can be written as follows for the case with $p_1 \neq 1$ and $p_2 \neq 1$:

$$\gamma_e = [\gamma_{e,\min}^{1-p_1} + A^{-1}(1-p_1)\xi]^{1/(1-p_1)} \quad (\text{for } \xi \leqslant \xi_{br}), \tag{A20}$$

$$\gamma_e = \left[\gamma_{e,br}^{1-p_2} - (1-p_2)\gamma_{e,br}^{p_1-p_2}\left(\frac{\gamma_{e,\min}^{1-p_1} - \gamma_{e,br}^{1-p_1}}{1-p_1} + A^{-1}\xi\right)\right]^{1/(1-p_2)} \quad (\text{for } \xi > \xi_{br}), \tag{A21}$$

where

$$\xi_{br} \equiv A\frac{\gamma_{e,br}^{1-p_1} - \gamma_{e,\min}^{1-p_1}}{1-p_1}, \tag{A22}$$

$$A \equiv \left[\frac{\gamma_{e,br}^{1-p_1} - \gamma_{e,\min}^{1-p_1}}{1-p_1} + \gamma_{e,br}^{-p_1+p_2}\frac{\gamma_{e,\max}^{1-p_2} - \gamma_{e,br}^{1-p_2}}{1-p_2}\right]^{-1}. \tag{A23}$$

For the case with $p_1 = 1$ and $p_2 \neq 1$,

$$\gamma_e = \gamma_{e,\min}\exp(A^{-1}\xi) \quad (\text{for } \xi \leqslant \xi_{br}), \tag{A24}$$

$$\gamma_e = \left\{\gamma_{e,br}^{1-p_2} - (1-p_2)\gamma_{e,br}^{p_1-p_2}\left[\ln\left(\frac{\gamma_{e,br}}{\gamma_{e,\min}}\right) - A^{-1}\xi\right]\right\}^{1/(1-p_2)} \quad (\text{for } \xi > \xi_{br}), \tag{A25}$$

where

$$\xi_{br} \equiv A\ln\left(\frac{\gamma_{e,br}}{\gamma_{e,\min}}\right), \tag{A26}$$

$$A \equiv \left[\ln\left(\frac{\gamma_{e,br}}{\gamma_{e,\min}}\right) + \gamma_{e,br}^{-p_1+p_2}\frac{\gamma_{e,\max}^{1-p_2} - \gamma_{e,br}^{1-p_2}}{1-p_2}\right]^{-1}. \tag{A27}$$

For the case with $p_1 \neq 1$ and $p_2 = 1$,

$$\gamma_e = [\gamma_{e,\min}^{1-p_1} + A^{-1}(1-p_1)\xi]^{1/(1-p_1)} (\text{for } \xi \leqslant \xi_{br}), \tag{A28}$$

$$\gamma_e = \gamma_{e,br}\exp\left[\gamma_{e,br}^{p_1-p_2}\left(A^{-1}\xi - \frac{\gamma_{e,br}^{1-p_1} - \gamma_{e,\min}^{1-p_1}}{1-p_1}\right)\right] \quad \text{for } (\xi > \xi_{br}), \tag{A29}$$

where

$$\xi_{br} \equiv A\frac{\gamma_{e,br}^{1-p_1} - \gamma_{e,\min}^{1-p_1}}{1-p_1}, \tag{A30}$$

$$A \equiv \left[\frac{\gamma_{e,br}^{1-p_1} - \gamma_{e,\min}^{1-p_1}}{1-p_1} + \gamma_{e,br}^{-p_1+p_2}\ln\left(\frac{\gamma_{e,\max}}{\gamma_{e,br}}\right)\right]^{-1}. \tag{A31}$$

A.2.4. Convergence Check of the MC Sampling

Here, we check the convergence of the MC sampling of the electron distribution functions.

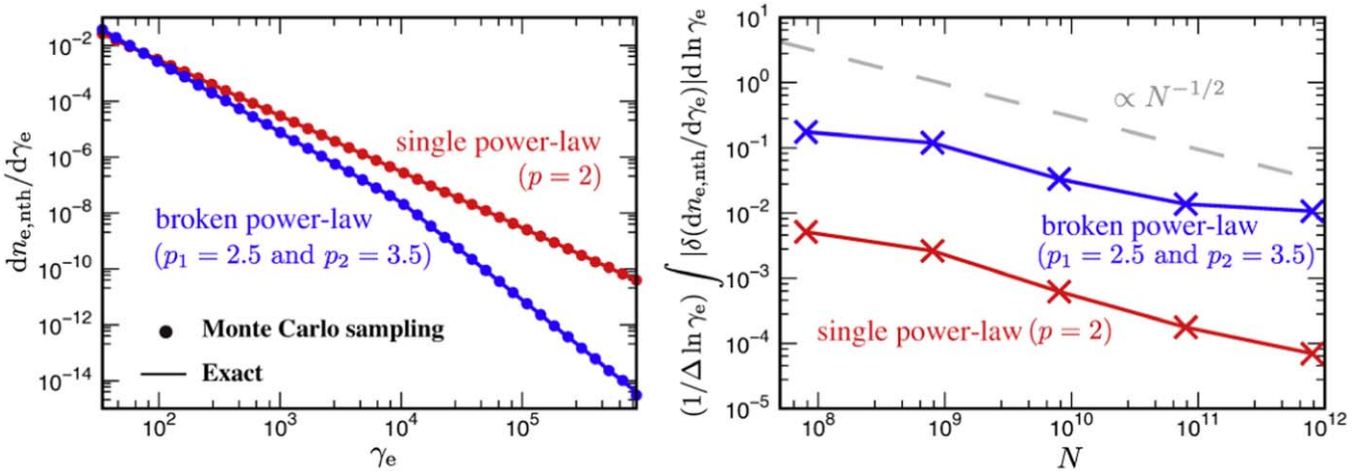

Figure 27. Left: nonthermal electron distribution functions with single power-law ($p = 2$) and broken power-law ($p_1 = 2.5$ and $p_2 = 3.5$) distributions. Filled circles and solid lines represent the result obtained by the MC sampling and the exact solutions described by the equation, respectively. The results of the dimensionless temparatures $\Theta_e = 10$ and 100 are displayed in blue and red, respectively. Right: integrated fractional errors as a function of the number of the MC-sampled electrons.

Figure 26 displays the distribution functions of the MC-sampled thermal electrons with dimensionless temperature $\Theta_e = 10$ and 100. For this convergence check, we evaluate the errors in the range of the electron Lorentz factor between 1 and $10\Theta_e$. In the left panel, one may find that the thermal electrons sampled by the MC method reproduce the Maxwell–Jüttner distributions well. The right panel shows the integrated fractional errors as a function of the number of the MC-sampled electrons. This represents the convergence of our MC sampling, whose errors are proportional to $N^{-1/2}$, where N is the number of sampled electrons.

The distribution functions of the MC-sampled nonthermal electrons with single and broken power-law distributions are shown in Figure 27. For the single power-law distribution, we set the power-law index $p = 2$ between $\gamma_{e,min}$ and $\gamma_{e,max}$. The electrons with the broken power-law distribution are set to have power-law indices with $p_1 = 2.5$ and $p_2 = 3.5$ in the range $\gamma_{e,min} \leqslant \gamma_e \leqslant \gamma_{e,br}$ and $\gamma_{e,br} < \gamma_e \leqslant \gamma_{e,max}$, respectively. Here, the minimum and maximum Lorentz factors of the electron distribution functions are $\gamma_{e,min} = 30$ and $\gamma_{max} = 10^6$ for the single and broken power-law distributions. The Lorentz factor of the break in the power law of the electron distribution is $\gamma_{e.\,br} = 10^4$. In the left panel, the nonthermal electrons sampled by the MC method reproduce the single and broken power-law distributions well. The integrated fractional errors of the MC sampling, whose errors are approximately proportional to $N^{-1/2}$, are shown in the right panel.

Appendix B
Emissivity

B.1. Formalism

B.1.1. Cyclo-synchrotron or Synchrotron via Thermal Electrons

For plasma with a mildly relativistic temperature, it is important to consider synchrotron emission taking into account the cyclotron emission. It is convenient to use the fitting formula for the angle-averaged cyclo-synchrotron emissivity (Mahadevan et al. 1996),

$$j^{(f)}_{\nu_f(cs)} = \frac{n_{e,th} e^2 \nu_f}{\sqrt{3}\, c K_2(\Theta_e^{-1})} M(x_{cs}), \tag{B1}$$

$$M(x_{cs}) \equiv \frac{4.0505}{x_{cs}^{1/6}}\left(1 + \frac{0.4}{x_{cs}^{1/4}} + \frac{0.5316}{x_{cs}^{1/2}}\right) \exp(-1.8899 x_{cs}^{1/3}), \tag{B2}$$

$$x_{cs} \equiv \frac{\nu_f}{\nu_{cs}}, \tag{B3}$$

$$\nu_{cs} \equiv \left(\frac{3eB}{4\pi m_e c}\right)\Theta_e^2. \tag{B4}$$

where K_2 is the modified Bessel function of the second kind, $n_{e,th}$ is the thermal electron density measured in the fluid rest frame, B is the magnetic field strength measured in the fluid rest frame, $\Theta_e (= k_B T_e / m_e c^2)$ is the dimensionless electron temperature, T_e is the electron temperature, k_B is the Boltzmann constant, m_e is the rest mass of the electron, and e is the elementary charge.

Alternatively, one can use the synchrotron formulation, which depends on the angle between the photon and the magnetic field measured in the fluid rest frame θ_B, for high-temperature plasma $\Theta \gtrsim 0.5$ (Leung et al. 2011),

$$j^{(f)}_{\nu_f(sy,th)} \simeq \frac{\sqrt{2}\pi n_{e,th} e^2 \nu_s}{3 c K_2(\Theta_e^{-1})}(x_s^{1/2} + 2^{11/12} x_s^{1/6})^2 \exp(-x_s^{1/3}), \tag{B5}$$

$$x_s \equiv \frac{\nu_f}{\nu_s}, \tag{B6}$$

$$\nu_s \equiv \frac{2}{9}\left(\frac{eB}{2\pi m_e c}\right)\Theta_e^2 \sin\theta_B, \tag{B7}$$

where

$$\cos\theta_B = -\frac{b^\mu p_{f\mu}}{B p_0^{(f)}}. \tag{B8}$$

B.1.2. Synchrotron via Nonthermal Electrons

Synchrotron emission via nonthermal electrons with single/broken power-law distribution functions are implemented.

The single power-law distribution $dn_{\rm e,nth}/d\gamma_e \propto \gamma_e^{-p}$ between the range $\gamma_{e,\rm min} \leqslant \gamma_e \leqslant \gamma_{e,\rm max}$ is written as

$$\frac{dn_{\rm e,nth}}{d\gamma_{\rm e}} = \frac{n_{\rm e,nth}(1-p)}{\gamma_{e,\rm max}^{1-p} - \gamma_{e,\rm min}^{1-p}}\gamma_{\rm e}^{-p} \ (\text{for } p \neq 1), \tag{B9}$$

$$\frac{dn_{\rm e,nth}}{d\gamma_{\rm e}} = \left[\ln\left(\frac{\gamma_{e,\rm max}}{\gamma_{e,\rm min}}\right)\right]^{-1}\gamma_{\rm e}^{-p} \ (\text{for } p = 1). \tag{B10}$$

The synchrotron emissivity is formulated as follows (see, e.g., Dexter et al. 2012; Dexter 2016):

$$j^{\rm (f)}_{\nu_{\rm f}(\rm sy,nth)} = \frac{(p-1)n_{\rm e,nth}e^2\nu_{\rm c}}{2\sqrt{3}\,c(\gamma_{e,\rm min}^{1-p} - \gamma_{e,\rm max}^{1-p})}\left(\frac{\nu_{\rm f}}{\nu_{\rm c}}\right)^{-(p-1)/2} \times [G(x_{\rm max}) - G(x_{\rm min})], \tag{B11}$$

$$G(x) = \int_x^\infty z^{(p-3)/2}F(z)dz, \tag{B12}$$

$$F(z) = z\int_z^\infty K_{5/3}(y)dy, \tag{B13}$$

where $\nu_{\rm c} = 3eB\sin\theta_B/(4\pi m_{\rm e}c)$, $x = \nu/(\gamma_{\rm e}^2\nu_{\rm c})$, and $x_{\rm min(max)} = \nu/(\gamma_{\rm e,min(max)}^2\nu_{\rm c})$.

The double integral in Equation (C2) can be reduced to the single integral (Westfold 1959)

$$\int_x^\infty dz z^{s-1}\int_z^\infty dy K_{t+1}(y) = \frac{s+t}{s}\int_x^\infty K_t(z) - \frac{x^s}{s} \times \left[\int_x^\infty K_{t+1}(y)dy - K_t(x)\right]. \tag{B14}$$

Alternatively, the broken power-law distribution function is also used to phenomenologically study the nonthermal emission, in which electrons with different power-law indices are distributed as $dn_{\rm e,nth}/d\gamma_e \propto \gamma_e^{-p_1}$ between the range $\gamma_{\rm e,min} \leqslant \gamma_e \leqslant \gamma_{\rm e,br}$ and $dn_{\rm e,nth}/d\gamma_e \propto \gamma_e^{-p_2}$ between the range $\gamma_{\rm e,br} < \gamma_{,\rm e} \leqslant \gamma_{\rm e\ max}$.

For $p_1 \neq 1$ and $p_2 \neq 1$,

$$\frac{dn_{\rm e,nth}}{d\gamma_{\rm e}} = {\rm A}n_{\rm e,nth}\gamma_{\rm e}^{-p_1} \ (\text{for } \gamma_{\rm e,min} \leqslant \gamma_{\rm e} \leqslant \gamma_{\rm e,br}), \tag{B15}$$

$$\frac{dn_{\rm e,nth}}{d\gamma_{\rm e}} = {\rm A}n_{\rm e,nth}\gamma_{\rm e,br}^{-p_1+p_2}\gamma_{\rm e}^{-p_2} \ (\text{for } \gamma_{\rm e,br} < \gamma_{\rm e} \leqslant \gamma_{\rm e,max}), \tag{B16}$$

where

$$A \equiv \left[\frac{\gamma_{\rm e,br}^{1-p_1} - \gamma_{\rm e,min}^{1-p_1}}{1-p_1} + \frac{\gamma_{\rm e,br}^{-p_1+p_2}(\gamma_{\rm e,max}^{1-p_2} - \gamma_{\rm e,br}^{1-p_2})}{1-p_2}\right]^{-1}. \tag{B17}$$

The synchrotron emissivity can be written as

$$j^{\rm (f)}_{\nu_{\rm f}(\rm sy,nth)} = A\frac{n_{\rm e,nth}e^2\nu_{\rm c}}{2\sqrt{3}\,c}\left\{\left(\frac{\nu_{\rm f}}{\nu_{\rm c}}\right)^{-(p_1-1)/2}[G(x_{\rm br}) - G(x_{\rm min})] + \gamma_{\rm e,br}^{-p_1+p_2}\left(\frac{\nu}{\nu_{\rm c}}\right)^{-(p_2-1)/2}[G(x_{\rm max}) - G(x_{\rm br})]\right\}, \tag{B18}$$

B.1.3. Bremsstrahlung via Thermal Electrons

For relativistic temperature plasma, electron-proton and electron-electron bremsstrahlung are both important. Here, we describe the bremsstrahlung emissivity via thermal electrons (see, e.g., Svensson 1982; Stepney & Guilbert 1983; Narayan & Yi 1995; Manmoto et al. 1997). The total bremsstrahlung emissivity $j^{\rm (f)}_{\nu_{\rm f}(\rm brms)}$ can be written as

$$j^{\rm (f)}_{\nu_{\rm f}(\rm brms)} = \frac{q^-_{\rm brms}f_{\rm Gaunt}}{4\pi}\exp\left(\frac{h\nu_{\rm f}}{k_{\rm B}T_{\rm e}}\right), \tag{B19}$$

where $f_{\rm Gaunt}$ is the Gaunt factor, given by

$$f_{\rm Gaunt} = \frac{h}{k_{\rm B}T_{\rm e}}\left(\frac{3}{\pi}\frac{k_{\rm B}T_{\rm e}}{h\nu_{\rm f}}\right)^{1/2}\left(\text{for } \frac{k_{\rm B}T_{\rm e}}{h\nu_{\rm f}} < 1\right), \tag{B20}$$

$$f_{\rm Gaunt} = \frac{h}{k_{\rm B}T_{\rm e}}\frac{\sqrt{3}}{\pi}\ln\left(\frac{4}{\zeta}\frac{k_{\rm B}T_{\rm e}}{h\nu_{\rm f}}\right)\left(\text{for } \frac{k_{\rm B}T_{\rm e}}{h\nu_{\rm f}} \geqslant 1\right), \tag{B21}$$

and the bremsstrahlung cooling rate per unit volume $q^-_{\rm brms}$ can be written as

$$q^-_{\rm brms} = q^-_{\rm brms,ep} + q^-_{\rm brms,ee}. \tag{B22}$$

Here, $q^-_{\rm brms,ep}$ and $q^-_{\rm brms,ee}$ are the rate for electron-proton and electron-electron bremsstrahlung, respectively. This can be formulated as follows:

$$q^-_{\rm brms,ep} = 1.25\, n^2_{\rm e,th}\sigma_{\rm T}\alpha_{\rm fs}m_{\rm e}c^3F_{\rm ep}(\Theta_{\rm e}), \tag{B23}$$

where $\alpha_{\rm fs}$ and $\sigma_{\rm T}$ are the fine-structure constant and the Thomsom-scattering cross section, and $F_{\rm ep}(\Theta_{\rm e})$ is

$$F_{\rm ep}(\Theta_{\rm e}) = 4\left(\frac{2\Theta_{\rm e}}{\pi^3}\right)^{1/2}(1 + 1.781\Theta_{\rm e}^{1.34}) \ (\text{for } \Theta_{\rm e} < 1), \tag{B24}$$

$$F_{\rm ep}(\Theta_{\rm e}) = \frac{9\Theta_{\rm e}}{2\pi}[\ln(1.123\Theta_{\rm e} + 0,48) + 1.5] \ (\text{for } \Theta_{\rm e} \geqslant 1), \tag{B25}$$

and

$$q^-_{\rm brms,ee} = n^2_{\rm e,th}r_{\rm e}^2\alpha_{\rm fs}c^3\frac{20}{9\pi^{1/2}}(44 - 3\pi^2)\Theta_{\rm e}^{3/2} \times (1 + 1.1\Theta_{\rm e} + \Theta_{\rm e}^2 - 1.25\Theta_{\rm e}^{5/2}) \ (\text{for } \Theta_{\rm e} < 1), \tag{B26}$$

$$q^-_{\rm brms,ee} = n^2_{\rm e,th}r_{\rm e}^2\alpha_{\rm fs}c^3 24\Theta_{\rm e}^{3/2}[\ln(1.1232\Theta_{\rm e}) + 1.28] \ (\text{for } \Theta_{\rm e} \geqslant 1), \tag{B27}$$

where $r_{\rm e}$ is the classical electron radius.

B.2. Methodology of the MC Sampling

In general, there are mainly two ways to sample the photon emissions with MC methods: (i) superphotons with a uniform weight are generated in such a way that their number is proportional to the emissivity of the plasma among the computational mesh, or (ii) the weight of superphotons is proportional to the emissivity with generating a uniform number of superphotons among the computational mesh.

We employ method (ii) because we consider various emission processes, i.e., thermal/nonthermal synchrotorn and bremsstrahlung emission. We can simply sum up the weight of superphotons when they are generated. The direction of the

generated superphotons is sampled to be isotropic using uniform pseudo-random numbers. It should be emphasized that the dependence of the synchrotron emissivity on the direction is automatically incorporated by this method, because the weight of superphotons is set to be proportional to the emissivity.

Our procedure is summarized as follows:

1. Superphotons are generated in such a way that their direction becomes isotropic in the fluid rest frame, using uniform pseudo-random numbers.
2. The weight of superphotons for each radiative process w, which is calculated with Equation (39), are summed up and the total weight of superphoton $w_{\rm tot}$ is comupted as follows:

$$w_{\rm tot} = \sum w, \tag{B28}$$

e.g., if we consider the synchrotron emission via thermal and nonthermal electrons and thermal bremsstrahlung emission, then

$$w_{\rm tot} = w_{\rm sy,th} + w_{\rm sy,nth} + w_{\rm brms}, \tag{B29}$$

where $w_{\rm sy,th}$, $w_{\rm sy,nth}$, and $w_{\rm brms}$ are the weight of superphotons generated by the synchrotron emission via thermal electrons, and the weight via nonthermal electrons, and bremsstrahlung, respectively.
3. The direction and energy of superphotons in the fluid rest frame are transformed into those in the observer frame to integrate the geodesic equations with the radiative processes (i.e., the general relativistic radiative transfer equations).

Appendix C
Absorption Coefficient

For the radiative processes via thermal electrons, the absorption coefficients are obtained by the Kirchhoff law, i.e.,

$$\alpha^{\rm (f)}_{\nu_{\rm f}} = \frac{j^{\rm (f)}_{\nu_{\rm f}}}{B_{\nu_{\rm f}}}, \tag{C1}$$

where $B_{\nu_{\rm f}}$ is the blackbody intensity of the plasma at which the radiative process takes place.

On the other hand, for the radiative processes via nonthermal electrons, the absorption coefficients are obtained by considering the more generalized picture of a detailed balance between emission and absorption with the Einstein relation including continuum states (see, e.g., Rybicki & Lightman 1979). The absorption coefficients for nonthermal electrons with a single-power law distribution is

$$\alpha^{\rm (f)}_{\nu_{\rm f}({\rm sy,nth})} = \frac{(p-1)(p+2)n_{\rm e,nth}e^2\nu_{\rm c}}{4\sqrt{3}\,c(\gamma_{e,\rm min}^{1-p} - \gamma_{e,\rm max}^{1-p})}\left(\frac{\nu_{\rm f}}{\nu_{\rm c}}\right)^{-(p+4)/2} \times [G_a(x_{\rm max}) - G_a(x_{\rm min})], \tag{C2}$$

$$G_a(x) = \int_x^\infty z^{(p-2)/2}F(z)dz, \tag{C3}$$

For nonthermal electrons with a broken power-law distribution, the absorption coefficient is represented as follows:

$$\alpha^{\rm (f)}_{\nu_{\rm f}({\rm sy,nth})} = A\frac{n_{\rm e,nth}e^2}{4\sqrt{3}\,m_{\rm e}c\nu_{\rm c}}\left\{(p_1+2)\left(\frac{\nu_{\rm f}}{\nu_{\rm c}}\right)^{-(p_1+4)/2} \times [G_a(x_{\rm br}) - G_a(x_{\rm min})] + (p_2+2)\gamma_{\rm e,br}^{-p_1+p_2}\left(\frac{\nu_{\rm f}}{\nu_{\rm c}}\right)^{-(p_2+4)/2}[G_a(x_{\rm max}) - G_a(x_{\rm br})]\right\}, \tag{C4}$$

where A is given in Equation (B17).

Appendix D
GRMHD Simulation Data

Three-dimensional GRMHD simulations are carried out by using GRRMHD simulation code UWABAMI in order to calculate the SEDs and images in Section 7. The radiation terms are not solved in this study because we focused on a low-mass accretion rate system, in which the two-temperature equations should be solved when we include radiation terms, and this is beyond the scope of this paper. The BH spin is set to be $a_* = 0.9375$. The inner- and outer-outflow boundaries are located at $1.18r_{\rm g}$ and $3.33\times10^3 r_{\rm g}$, respectively, where the former appears inside the event horizon of the BH $r_{\rm H} = (1+\sqrt{1-a_*^2})r_{\rm g} \simeq 1.35r_{\rm g}$. The simulation domain is divided into $(N_r, N_\theta, N_\varphi) = (192, 120, 96)$ meshes, where N_r, N_θ, and N_φ are the numbers of meshes in the r, θ, and φ direction of the modified Kerr-Schild coordinate.

Initially, we set an isentropic hydroequilibrium torus rotating around the Kerr BH (Fishbone & Moncrief 1976), which is embeded in a hot, static, uniform, and non-magnetized ambient gas. The position of the inner edge and the pressure maximum of the torus are set at $r = 20r_{\rm g}$ and $r = 33r_{\rm g}$ on the equatorial plane, respectively. The specific heat ratio is assumed to be $\gamma_{\rm heat} = 13/9$. After the growth of the magneto-rotational instability (Balbus & Hawley 1991), the accretion flow is formed via the angular momentum transport. We use the snapshot at $t = 1.2\times10^4 r_{\rm g}/c$, in which the accretion flow is in quasi-steady state. The structure of the accretion flow at $t = 1.2\times10^4 r_{\rm g}/c$ is displayed in Figure 28.

The accretion flow is roughly categorized into two states by the magnitude of their magnetization: standard and normal evolution (SANE) and magnetically arrested disk (MAD), which are weakly and strongly magnetized states, respectively (e.g., Narayan et al. 2012; Sadowski et al. 2013; Tchekhovskoy 2015; Event Horizon Telescope Collaboration 2019e, and references therein). SANE and MAD are defined by the dimensionless magnetic flux threading the event horizon, which is described as

$$\phi_{\rm BH} = \frac{\Phi_{\rm BH}}{\sqrt{\dot{M}_{\rm BH}r_{\rm g}c}}, \tag{D1}$$

where the magnetic flux $\Phi_{\rm BH}$ and the mass accretion rate onto the BH $\dot{M}_{\rm BH}$ is

$$\Phi_{\rm BH} = \frac{1}{2}\int_\theta\int_\varphi |B^r|dA_{\theta\varphi}, \tag{D2}$$

$$\dot{M}_{\rm BH} = \int_\theta\int_\varphi \rho u^r dA_{\theta\varphi}. \tag{D3}$$

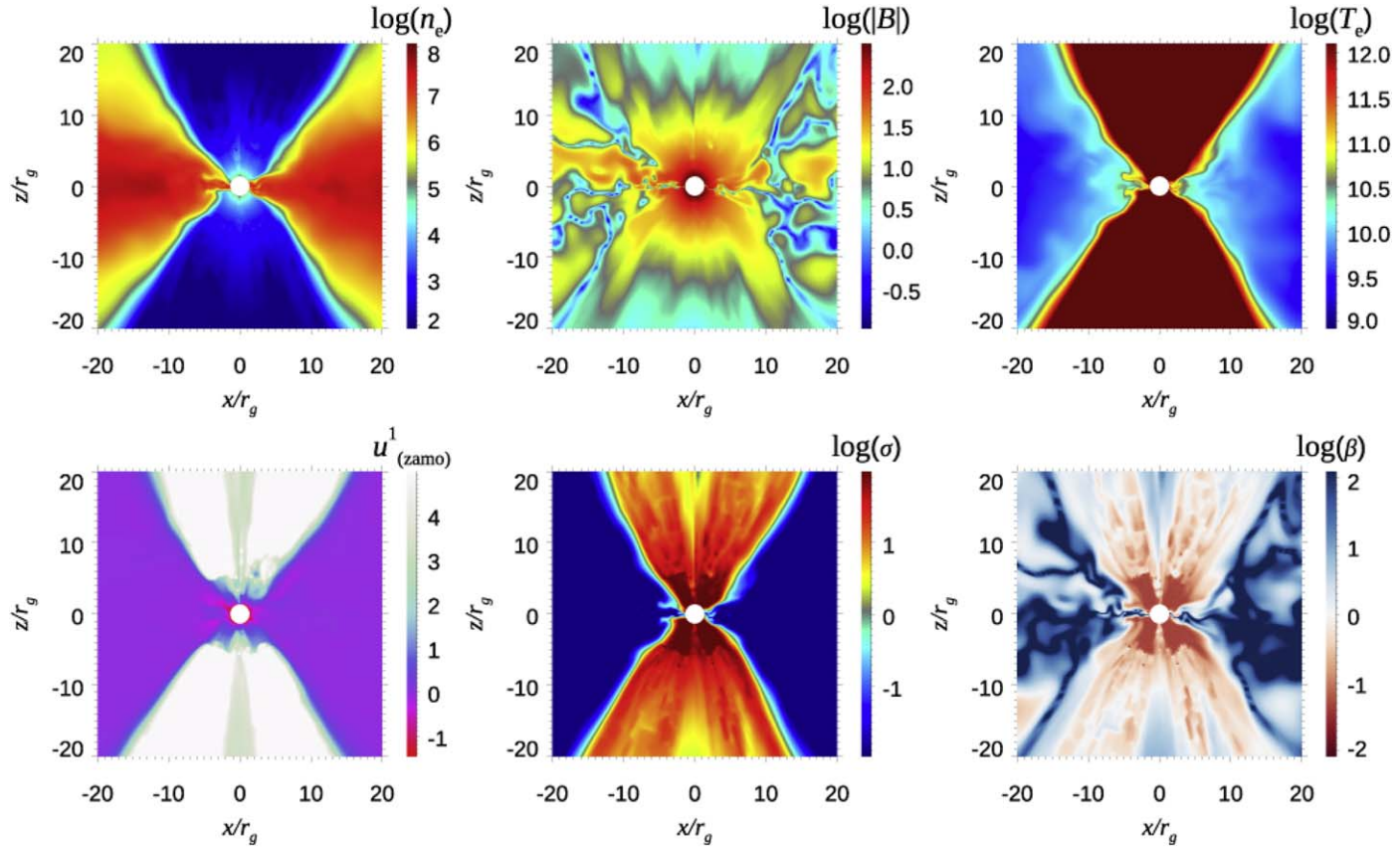

Figure 28. Spatial distribution of electron number density (top left), magnetic field strength (top middle), electron temperature (top right), radial component of the four-velocity in the ZAMO frame (bottom left), magnetization $\sigma = B^2/\rho c^2$ (bottom middle), and plasma-β (bottom right).

Here, $dA_{\theta\varphi} = \sqrt{-g}\,d\theta d\varphi$ is an area element in the θ–φ plane, and g is the determinant of the Kerr-Schild metric. In SANE and MAD states, $\Phi_{\rm BH} \sim 1$, and $\sim$15, respectively. The normalized magnetic flux is $\Phi_{\rm BH} \approx 5$ in our simulation, so that the accretion flow is categorized into the state between SANE and MAD, which is sometimes referred to as semi-MAD[9], although the magnetic flux is slightly high.

ORCID iDs

Tomohisa Kawashima https://orcid.org/0000-0001-8527-0496
Ken Ohsuga https://orcid.org/0000-0002-2309-3639
Hiroyuki R. Takahashi https://orcid.org/0000-0003-0114-5378

References

Abramowicz, M. A., Czerny, B., Lasota, J. P., & Szuszkiewicz, E. 1988, ApJ, 332, 646
Aleksić, J., Ansoldi, S., Antonelli, L. A., et al. 2014, Sci, 346, 1080
Balbus, S. A., & Hawley, J. F. 1991, ApJ, 376, 214
Ball, D., Özel, F., Psaltis, D., & Chan, C.-k. 2016, ApJ, 826, 77
Bardeen, J. M. 1973, in Black Holes (Les Astres Occlus), ed. C. Dewitt & B. S. Dewitt (New York: Gordon and Breach), 215
Bardeen, J. M., Press, W. H., & Teukolsky, S. A. 1972, ApJ, 178, 347
Blandford, R. D., & Payne, D. G. 1982, MNRAS, 199, 883
Blandford, R. D., & Znajek, R. L. 1977, MNRAS, 179, 433
Broderick, A. E., & Loeb, A. 2006, MNRAS, 367, 905
Canfield, E., Howard, W. M., & Liang, E. P. 1987, ApJ, 323, 565
Chael, A., Johnson, M. D., & Lupsasca, A. 2021, ApJ, 918, 6
Chael, A. A., Johnson, M. D., Bouman, K. L., et al. 2018, ApJ, 857, 23
Chael, A. A., Johnson, M. D., Narayan, R., et al. 2016, ApJ, 829, 11
Chael, A. A., Narayan, R., & Saowski, A. 2017, MNRAS, 470, 2367
Chan, C.-K., Psaltis, D., Özel, F., Narayan, R., & Saowski, A. 2015, ApJ, 799, 1
Chandrasekhar, S. 1983, The Mathematical Theory of Black Holes (Oxford: Clarendon Press)
Chatterjee, K., Markoff, S., Neilsen, J., et al. 2021, MNRAS, 507, 5281
Cho, I., Zhao, G.-Y., Kawashima, T., et al. 2022, ApJ, 926, 108
Curd, B., & Narayan, R. 2019, MNRAS, 483, 565
Davelaar, J., Mościbrodzka, M., Bronzwaer, T., & Falcke, H. 2018, A&A, 612, A34
Davis, S. W., Blaes, O. M., Hirose, S., & Krolik, J. H. 2009, ApJ, 703, 569
Dexter, J. 2016, MNRAS, 462, 115
Dexter, J., McKinney, J. C., & Agol, E. 2012, MNRAS, 421, 1517
Dolence, J. C., Gammie, C. F., Mościbrodzka, M., & Leung, P. K. 2009, ApJS, 184, 387
EHT MWL Science Working Group, Algaba, J. C., Anczarski, J., et al. 2021, ApJL, 911, L11
Event Horizon Telescope Collaboration, Akiyama, K., Alberdi, A., et al. 2022, ApJL, 930, L16
Event Horizon Telescope Collaboration, Akiyama, K., Alberdi, A., et al. 2019a, ApJL, 875, L1
Event Horizon Telescope Collaboration, Akiyama, K., Alberdi, A., et al. 2019b, ApJL, 875, L2
Event Horizon Telescope Collaboration, Akiyama, K., Alberdi, A., et al. 2019c, ApJL, 875, L3
Event Horizon Telescope Collaboration, Akiyama, K., Alberdi, A., et al. 2019d, ApJL, 875, L4
Event Horizon Telescope Collaboration, Akiyama, K., Alberdi, A., et al. 2019e, ApJL, 875, L5
Event Horizon Telescope Collaboration, Akiyama, K., Alberdi, A., et al. 2019f, ApJL, 875, L6
Event Horizon Telescope Collaboration, Akiyama, K., Algaba, J. C., et al. 2021, ApJL, 910, L13
Falcke, H., Melia, F., & Agol, E. 2000, ApJL, 528, L13

[9] This corresponds to the normalized magnetic flux $\approx$18 in the formulation in Tchekhovskoy et al. (2011), in which the magnetic flux is multiplied by $\sqrt{4\pi}$.

Fishbone, L. G., & Moncrief, V. 1976, ApJ, 207, 962
Gold, R., Broderick, A. E., Younsi, Z., et al. 2020, ApJ, 897, 148
Gold, R., McKinney, J. C., Johnson, M. D., & Doeleman, S. S. 2017, ApJ, 837, 180
Gorecki, A., & Wilczewski, W. 1984, AcA, 34, 141
Hayashida, K., Asakura, K., Ishikura, A., et al. 2020, Proc. SPIE, 11444, 114441C
Johannsen, T. 2013, ApJ, 777, 170
Johnson, M. D., Lupsasca, A., Strominger, A., et al. 2020, SciA, 6, eaaz1310
Kawanaka, N., Kato, Y., & Mineshige, S. 2008, PASJ, 60, 399
Kawanaka, N., & Mineshige, S. 2021, PASJ, 73, 630
Kawashima, T., Kino, M., & Akiyama, K. 2019, ApJ, 878, 27
Kawashima, T., Ohsuga, K., Mineshige, S., et al. 2012, ApJ, 752, 18
Kawashima, T., Toma, K., Kino, M., et al. 2021, ApJ, 909, 168
Kitaki, T., Mineshige, S., Ohsuga, K., & Kawashima, T. 2017, PASJ, 69, 92
Kompaneets, A. S. 1957, JETP, 4, 730
Leung, P. K., Gammie, C. F., & Noble, S. C. 2011, ApJ, 737, 21
Luminet, J.-P. 1979, A&A, 75, 228
Lynden-Bell, D. 1996, MNRAS, 279, 389
MAGIC Collaboration, Acciari, V. A., Ansoldi, S., et al. 2020, MNRAS, 492, 5354
MAGIC Collaboration, Albert, J., Aliu, E., et al. 2008, Sci, 320, 1752
Mahadevan, R., Narayan, R., & Yi, I. 1996, ApJ, 465, 327
Manmoto, T., Mineshige, S., & Kusunose, M. 1997, ApJ, 489, 791
Mao, S. A., Dexter, J., & Quataert, E. 2017, MNRAS, 466, 4307
Massaro, E., Tramacere, A., Perri, M., Giommi, P., & Tosti, G. 2006, A&A, 448, 861
Mościbrodzka, M., Dexter, J., Davelaar, J., & Falcke, H. 2017, MNRAS, 468, 2214
Mościbrodzka, M., Falcke, H., & Shiokawa, H. 2016, A&A, 586, A38
Mościbrodzka, M., Gammie, C. F., Dolence, J. C., Shiokawa, H., & Leung, P. K. 2009, ApJ, 706, 497
Narayan, R., SÄ dowski, A., Penna, R. F., & Kulkarni, A. K. 2012, MNRAS, 426, 3241
Narayan, R., SaÌ§dowski, A., & Soria, R. 2017, MNRAS, 469, 2997
Narayan, R., & Yi, I. 1994, ApJL, 428, L13
Narayan, R., & Yi, I. 1995, ApJ, 452, 710
Noble, S. C., Leung, P. K., Gammie, C. F., & Book, L. G. 2007, CQGra, 24, S259
Ohsuga, K., Kato, Y., & Mineshige, S. 2005, ApJ, 627, 782
Özel, F., Psaltis, D., & Narayan, R. 2000, ApJ, 541, 234
Pozdnyakov, L. A., Sobol, I. M., & Syunyaev, R. A. 1977, SvA, 21, 708
Pozdnyakov, L. A., Sobol, I. M., & Syunyaev, R. A. 1983, ASPRv, 2, 189
Press, W. H., Teukolsky, S. A., Vetterling, W. T., & Flannery, B. P. 2002, Numerical recipes in C++ : the art of scientific computing (Cambridge: Cambridge Univ. Press)
Psaltis, D., Özel, F., Chan, C.-K., & Marrone, D. P. 2015, ApJ, 814, 115
Pu, H.-Y., Akiyama, K., & Asada, K. 2016a, ApJ, 831, 4
Pu, H.-Y., Yun, K., Younsi, Z., & Yoon, S.-J. 2016b, ApJ, 820, 105
Quataert, E. 2002, ApJ, 575, 855
Rees, M. J. 1984, ARA&A, 22, 471
Rybicki, G. B., & Lightman, A. P. 1979, Radiative processes in astrophysics (New York: Wiley)
Scepi, N., Dexter, J., & Begelman, M. C. 2022, MNRAS, 511, 3536
Schnittman, J. D., & Krolik, J. H. 2013, ApJ, 777, 11
Schnittman, J. D., Krolik, J. H., & Noble, S. C. 2013, ApJ, 769, 156
Shakura, N. I., & Sunyaev, R. A. 1973, A&A, 500, 33
Shcherbakov, R. V., Penna, R. F., & McKinney, J. C. 2012, ApJ, 755, 133
Sikora, M. 1981, MNRAS, 196, 257
Sądowski, A., Narayan, R., Penna, R., & Zhu, Y. 2013, MNRAS, 436, 3856
Stepney, S., & Guilbert, P. W. 1983, MNRAS, 204, 1269
Svensson, R. 1982, ApJ, 258, 335
Takahashi, H. R., Ohsuga, K., Kawashima, T., & Sekiguchi, Y. 2016, ApJ, 826, 23
Takahashi, R. 2004, ApJ, 611, 996
Tchekhovskoy, A. 2015, in The Formation and Disruption of Black Hole Jets, ed. I. Contopoulos, D. Gabuzda, & N. Kylafis, Vol. 414 (Berlin: Springer), 45
Tchekhovskoy, A., Narayan, R., & McKinney, J. C. 2011, MNRAS Lett., 418, L79
Tramacere, A., Giommi, P., Perri, M., Verrecchia, F., & Tosti, G. 2009, A&A, 501, 879
Tramacere, A., Massaro, E., & Taylor, A. M. 2011, ApJ, 739, 66
Tsunetoe, Y., Mineshige, S., Ohsuga, K., Kawashima, T., & Akiyama, K. 2020, PASJ, 72, 32
Tsunetoe, Y., Mineshige, S., Ohsuga, K., Kawashima, T., & Akiyama, K. 2021, PASJ, 73, 912
Uttley, P., Hartog, R. d., Bambi, C., et al. 2021, ExA, 51, 1081
Volonteri, M. 2012, Sci, 337, 544
Westfold, K. C. 1959, ApJ, 130, 241
Wong, G. N. 2021, ApJ, 909, 217
Wong, G. N., Ryan, B. R., & Gammie, C. F. 2021, ApJ, 907, 73
Yarza, R., Wong, G. N., Ryan, B. R., & Gammie, C. F. 2020, ApJ, 898, 50
Younsi, Z., Wu, K., & Fuerst, S. V. 2012, A&A, 545, A13
Yuan, F., & Narayan, R. 2014, ARA&A, 52, 529
Yuan, F., Quataert, E., & Narayan, R. 2003, ApJ, 598, 301